HAL
open science

Testing the universality of the star-formation efficiency in dense molecular gas

Y. Shimajiri, Ph. André, J. Braine, V. Könyves, N. Schneider, Sylvain Bontemps, B. Ladjelate, A. Roy, Y. Gao, H. Chen

To cite this version:

Y. Shimajiri, Ph. André, J. Braine, V. Könyves, N. Schneider, et al.. Testing the universality of the star-formation efficiency in dense molecular gas. Astronomy and Astrophysics - A&A, 2017, 604, pp.A74. 10.1051/0004-6361/201730633 . hal-01518282

HAL Id: hal-01518282

https://hal.science/hal-01518282v1

Submitted on 6 Oct 2020

HAL is a multi-disciplinary open access archive for the deposit and dissemination of scientific research documents, whether they are published or not. The documents may come from teaching and research institutions in France or abroad, or from public or private research centers.

L'archive ouverte pluridisciplinaire **HAL**, est destinée au dépôt et à la diffusion de documents scientifiques de niveau recherche, publiés ou non, émanant des établissements d'enseignement et de recherche français ou étrangers, des laboratoires publics ou privés.

A&A 604, A74 (2017)
DOI: 10.1051/0004-6361/201730633
© ESO 2017

Astronomy & Astrophysics

Testing the universality of the star-formation efficiency in dense molecular gas★

Y. Shimajiri[1], Ph. André[1], J. Braine[2], V. Könyves[1], N. Schneider[3], S. Bontemps[2], B. Ladjelate[1], A. Roy[1], Y. Gao[4,5], and H. Chen[6,7,8]

[1] Laboratoire AIM, CEA/DSM-CNRS-Université Paris Diderot, IRFU/Service d'Astrophysique, CEA Saclay, 91191 Gif-sur-Yvette, France
e-mail: yoshito.shimajiri@cea.fr
[2] Laboratoire d'Astrophysique de Bordeaux, Univ. Bordeaux, CNRS, B18N, Allée Geoffroy Saint-Hilaire, 33615 Pessac, France
[3] I. Physik. Institut, University of Cologne, Zülpicher Str. 77, 50937 Koeln, German
[4] Purple Mountain Observatory, Chinese Academy of Sciences, 2 West Beijing Road, 210008 Nanjing, PR China
[5] Key Laboratory of Radio Astronomy, Chinese Academy of Sciences, 210008 Nanjing, PR China
[6] School of Astronomy and Space Science, Nanjing University, 210093 Nanjing, PR China
[7] Key Laboratory of Modern Astronomy and Astrophysics, Nanjing University, 210093 Nanjing, PR China
[8] Collaborative Innovation Center of Modern Astronomy and Space Exploration, 210093 Nanjing, PR China

Received 15 February 2017 / Accepted 25 April 2017

ABSTRACT

Context. Recent studies with, for example, *Spitzer* and *Herschel* have suggested that star formation in dense molecular gas may be governed by essentially the same "law" in Galactic clouds and external galaxies. This conclusion remains controversial, however, in large part because different tracers have been used to probe the mass of dense molecular gas in Galactic and extragalactic studies.

Aims. We aimed to calibrate the HCN and HCO^+ lines commonly used as dense gas tracers in extragalactic studies and to test the possible universality of the star-formation efficiency in dense gas ($\gtrsim 10^4$ cm^{-3}), SFE_{dense}.

Methods. We conducted wide-field mapping of the Aquila, Ophiuchus, and Orion B clouds at ~0.04 pc resolution in the $J = 1–0$ transition of HCN, HCO^+, and their isotopomers. For each cloud, we derived a reference estimate of the dense gas mass $M_{Herschel}^{A_V>8}$, as well as the strength of the local far-ultraviolet (FUV) radiation field, using *Herschel* Gould Belt survey data products, and estimated the star-formation rate from direct counting of the number of *Spitzer* young stellar objects.

Results. The $H^{13}CO^+$(1–0) and $H^{13}CN$(1–0) lines were observed to be good tracers of the dense star-forming filaments detected with *Herschel*. Comparing the luminosities L_{HCN} and L_{HCO^+} measured in the HCN and HCO^+ lines with the reference masses $M_{Herschel}^{A_V>8}$, the empirical conversion factors $\alpha_{Herschel-HCN}$ ($=M_{Herschel}^{A_V>8}/L_{HCN}$) and $\alpha_{Herschel-HCO^+}$ ($=M_{Herschel}^{A_V>8}/L_{HCO^+}$) were found to be significantly anti-correlated with the local FUV strength. In agreement with a recent independent study of Orion B by Pety et al., the HCN and HCO^+ lines were found to trace gas down to $A_V \gtrsim 2$. As a result, published extragalactic HCN studies must be tracing all of the moderate density gas down to $n_{H_2} \lesssim 10^3$ cm^{-3}. Estimating the contribution of this moderate density gas from the typical column density probability distribution functions in nearby clouds, we obtained the following G_0-dependent HCN conversion factor for external galaxies: $\alpha_{Herschel-HCN}^{fit'} = 64 \times G_0^{-0.34}$. Re-estimating the dense gas masses in external galaxies with $\alpha_{Herschel-HCN}^{fit'}(G_0)$, we found that SFE_{dense} is remarkably constant, with a scatter of less than 1.5 orders of magnitude around 4.5×10^{-8} yr^{-1}, over eight orders of magnitude in dense gas mass.

Conclusions. Our results confirm that SFE_{dense} of galaxies is quasi-universal on a wide range of scales from ~1–10 pc to >10 kpc. Based on the tight link between star formation and filamentary structure found in *Herschel* studies of nearby clouds, we argue that SFE_{dense} is primarily set by the "microphysics" of core and star formation along filaments.

Key words. ISM: clouds – stars: formation

1. Introduction

A close connection between dense molecular gas (with $n_{H_2} > 10^4$ cm^{-3}) and star formation has been established for quite some time on both Galactic and extragalactic scales. On small scales, individual stars of low to intermediate masses are known to form from the collapse of prestellar dense cores (e.g., Myers 1983; Ward-Thompson et al. 1994; André et al. 2000), themselves often embedded in dense cluster-forming gas clumps within molecular clouds (e.g., Lada 1992; Myers 1998). On galaxy-wide scales, the global star-formation rate (SFR) is linearly correlated with the total amount of dense molecular gas as traced by HCN observations (Gao & Solomon 2004a,b), while the correlation between the SFR and the amount of either atomic (HI) or low-density molecular (CO) gas is non linear and not as tight (e.g., Kennicutt 1989). Moreover, as pointed out by Lada et al. (2012), essentially the same relation between SFR and mass of dense gas M_{dense} is found in nearby Galactic clouds ($SFR = 4.6 \times 10^{-8}\ M_\odot\,yr^{-1} \times (M_{dense}/M_\odot)$ – Lada et al. 2010) and external galaxies ($SFR = 2 \times 10^{-8}\ M_\odot\,yr^{-1} \times (M_{dense}/M_\odot)$ – Gao & Solomon 2004b). The only exception seems to be the extreme star-forming environment of the central molecular zone (CMZ) of our Galaxy, where a very low star-formation efficiency

★ Partly based on observations carried out with the IRAM 30 m Telescope under project numbers 150-14 and 032-15. IRAM is supported by INSU/CNRS (France), MPG (Germany) and IGN (Spain).

in dense gas has been reported (Longmore et al. 2013). Investigating the nature and origin of this quasi-universal "star formation law" in the dense molecular gas of galaxies is of fundamental importance for our understanding of star formation and galaxy evolution in the Universe.

Key insight is provided by the results of recent submillimeter imaging surveys of Galactic molecular clouds with the *Herschel* Space Observatory, which emphasize the role of interstellar filaments in the star formation process (e.g., André et al. 2010; Molinari et al. 2010). The presence of filamentary structures in molecular clouds was already known long before *Herschel* (e.g., Schneider & Elmegreen 1979; Myers 2009), but *Herschel* observations now demonstrate that molecular filaments are truly ubiquitous, make up a dominant fraction of the dense gas in molecular clouds, and present a high degree of universality in their properties (e.g., Arzoumanian et al. 2011; Hill et al. 2011; Schisano et al. 2014; Könyves et al. 2015). A detailed analysis of the radial column density profiles of nearby *Herschel* filaments shows that they are characterized by a narrow distribution of central widths with a typical full width at half maximum (FWHM) value of ~0.1 pc and a dispersion of less than a factor of two (Arzoumanian et al. 2011). Another major result from the *Herschel* Gould Belt survey (HGBS – André et al. 2010) is that the vast majority of prestellar cores are found in dense, "supercritical" filaments for which the mass per unit length exceeds the critical line mass of nearly isothermal, long cylinders (e.g., Inutsuka & Miyama 1997), $M_{\rm line,crit} = 2\,c_{\rm s}^2/G \sim 16\ M_\odot\,{\rm pc}^{-1}$, where $c_{\rm s} \sim 0.2$ km s^{-1} is the isothermal sound speed for molecular gas at $T \sim 10$ K (e.g., Könyves et al. 2015). These *Herschel* findings in nearby Galactic clouds support a scenario of star formation in two main steps (cf. André et al. 2014): first, large-scale compression of interstellar material in supersonic flows (turbulent or not) generates a quasi-universal web of filaments in the cold interstellar medium (ISM); second, the densest filaments fragment into prestellar cores (and subsequently protostars) by gravitational instability above $M_{\rm line,crit}$.

The realization that, at least in nearby clouds, prestellar core formation occurs primarily along dense filaments of roughly constant inner width has potential implications for our understanding of star formation on global galactic scales. Remarkably, the critical line mass of a filament, $M_{\rm line,crit} = 2\,c_{\rm s}^2/G$, depends only on gas temperature (i.e., $T \sim 10$ K for the bulk of Galactic molecular clouds, away from the immediate vicinity of massive stars). Given the common filament width $W_{\rm fil} \sim 0.1$ pc (Arzoumanian et al. 2011) this may set a quasi-universal threshold for core/star formation in the giant molecular clouds (GMCs) of galaxies at $M_{\rm line,crit} \sim 16\ M_\odot$ pc^{-1} in terms of filament mass per unit length, or $M_{\rm line,crit}/W_{\rm fil} \sim 160\ M_\odot$ pc^{-2} in terms of gas surface density (corresponding to a visual extinction $A_{\rm V} \sim 8$), or $M_{\rm line,crit}/W_{\rm fil}^2 \sim 1600\ M_\odot$ pc^{-3} in terms of gas density (i.e., a number density $n_{\rm H_2} \sim 2.3 \times 10^4$ cm^{-3}). Indeed, independent *Spitzer* infrared studies of the SFR as a function of gas surface density in nearby cloud complexes (e.g., Heiderman et al. 2010; Lada et al. 2010; Evans et al. 2014) show that the SFR tends to be linearly proportional to the mass of dense gas above a surface density threshold $\Sigma_{\rm gas}^{\rm th} \sim 130\ M_\odot$ pc^{-2} and drops to negligible values below $\Sigma_{\rm gas}^{\rm th}$. The observed star formation threshold $\Sigma_{\rm gas}^{\rm th}$ corresponds to within a factor of $\ll$2 to the line-mass threshold above which interstellar filaments are expected to be gravitationally unstable.

While the observational results summarized above are very encouraging and tentatively point to a unified picture for star formation on GMC scales in both Galactic clouds and external galaxies, there are at least two caveats. First, direct comparison between Galactic (e.g., Lada et al. 2010) and extragalactic (e.g., Gao & Solomon 2004b) studies of the dense gas – star formation connection is difficult at this stage because different tracers have been used to probe dense gas in Galactic and extragalactic situations so far. For instance, Lada et al. (2010) used column density maps from near-infrared extinction and derived the total mass $M_{\rm dense}^{A_{\rm V}>8}$ above the extinction/surface density threshold mentioned earlier (i.e., $A_{\rm V} > 8$), while Gao & Solomon (2004b) used HCN (1–0) data and estimated the mass of dense gas $M_{\rm dense}$ above the effective density $\sim 3 \times 10^4$ cm^{-3} of the HCN (1–0) transition from the HCN (1–0) line luminosity, i.e., $M_{\rm dense}^{\rm HCN} = \alpha_{\rm GS04-HCN}\ L_{\rm HCN}$ with $\alpha_{\rm GS04-HCN} \sim 10\ M_\odot\ ({\rm K\,km\,s^{-1}\,pc^2})^{-1}$ (see also Wu et al. 2005). While the effective density of the HCN(1–0) transition (cf. Evans 1999) turns out to be close to the critical threshold density $\sim 2.3 \times 10^4$ cm^{-3} quoted above for ~0.1-pc-wide supercritical filaments, the relation between $M_{\rm dense}^{A_{\rm V}>8}$ and $M_{\rm dense}^{\rm HCN}$ remains to be properly calibrated in nearby Galactic clouds. Second, significant variations in the apparent star-formation efficiency in dense gas $SFE_{\rm dense}^{\rm extragal} \equiv L_{\rm FIR}/L_{\rm HCN}$ as a function of stellar surface density or galactocentric radius have been found in resolved observations of the disks of several nearby galaxies (Usero et al. 2015; Chen et al. 2015; Leroy et al. 2016; Bigiel et al. 2016). To confirm that there is a universal star formation law converting the dense molecular gas of GMCs into stars, wide-field line mapping observations of Galactic clouds in the same dense gas tracers as used in extragalactic work and at a spatial resolution high enough to resolve ~0.1-pc-wide molecular filaments are crucially needed.

With the advent of sensitive heterodyne receivers and wideband spectrometers on millimeter-wave telescopes, wide-field mapping observations in several lines simultaneously are now feasible at an angular resolution down to ~10–30″. In this paper, we present wide-field imaging data in the HCN (1–0), $H^{13}CN$ (1–0), HCO^+ (1–0), and $H^{13}CO^+$ (1–0) transitions toward three nearby star-forming clouds, Aquila, Ophiuchus, and Orion B. The paper is organized as follows. In Sect. 2, we describe our IRAM 30 m, MOPRA 22 m, and Nobeyama 45 m observations. In Sect. 3, we present the results of the HCN, $H^{13}CN$, HCO^+, and $H^{13}CO^+$ mappings and estimate the far ultraviolet (FUV) field strength from *Herschel* HGBS 70 μm and 100 μm data. In Sect. 4, we discuss evidence of significant variations in the conversion factor $\alpha_{\rm HCN}$ between HCN luminosity and mass of dense gas, and, in particular, the dependence of $\alpha_{\rm HCN}$ on the FUV field strength. We then revisit the question of the universality of the star-formation efficiency in the dense molecular gas of galaxies and propose an interpretation of this universality in terms of the filamentary structure of GMCs. Our conclusions are summarized in Sect. 5.

2. Millimeter line observations

We carried out observations in the HCN (J = 1–0, 88.6318473 GHz), $H^{13}CN$ (J = 1–0, 86.340167 GHz), HCO^+ (J = 1–0, 89.188526 GHz), and $H^{13}CO^+$ (J = 1–0, 86.75433 GHz) transitions toward three nearby star-forming regions, Aquila, Ophiuchus, and Orion B using the IRAM 30 m, MOPRA 22 m, and Nobeyama 45 m telescopes. The effective excitation densities[1] of the HCN (1–0), $H^{13}CN$ (1–0), HCO^+ (1–0), and $H^{13}CO^+$ (1–0) lines at 10 K are 8.4×10^3 cm^{-3},

[1] The effective excitation density of a molecular transition at a given gas kinetic temperature is defined as the density which results in a spectral line with an integrated intensity of 1 K km s^{-1} (Shirley 2015).

Table 1. Observations.

Region	Aquila	Ophiuchus	Orion B
Distance	260 pc*	139 pc†	400 pc‡
Telescope	IRAM 30 m	MOPRA 22 m	Nobeyama 45 m
Receiver	EMIR	3 mm	TZ
Correlator	FTS50	MOPS	SAM45
Obs. period	18–29 Dec. 2014 2–9 Sep. 2015	26 July–2 Aug. 2015	7–21 May 2015
Mapping area	0.42 deg^2 (~8.7 pc^2)	0.21 deg^2 (~1.2 pc^2)	0.14 deg^2 (~6.8 pc^2)
$\theta_{\rm ant}$ at 86 GHz	28.″6 (~0.04 pc)	39.″0 (~0.03 pc)	19.″1 (~0.04 pc)
dV at 86 GHz	0.15 km s^{-1}	0.10 km s^{-1}	0.023 km s^{-1}

Notes. (*) The distance to the Aquila molecular complex is under debate (Drew et al. 1997; Dzib et al. 2010; Ortiz-León et al. 2017). In this paper, we adopt a distance of 260 pc for Aquila according to Maury et al. (2011) and Könyves et al. (2015). (†) See Mamajek (2008). (‡) See Gibb (2008).

3.5×10^5 cm^{-3}, 9.5×10^2 cm^{-3}, and 3.9×10^4 cm^{-3}, respectively (Shirley 2015). Table 1 shows a summary of our molecular line observations. We describe the details of each observation below.

2.1. IRAM 30 m observations toward the Aquila cloud

During two observing runs (18 December 2014–29 December 2014 and 2 September 2015–9 September 2015), we carried out mapping observations toward a 0.4 deg^2 region in the Aquila cloud, including the three subregions Aquila/W40, Aquila/Serp. South, and Aquila/cold (see Figs. 1 and A.1), with the Eight MIxer Receiver (EMIR) receiver on the IRAM-30 m telescope. All molecular line data were obtained simultaneously. At 86 GHz, the 30 m telescope has a beam size of 28.6″ (HPBW) and the forward and main beam efficiencies ($F_{\rm eff}$ and $B_{\rm eff}$) are 95% and 81%. As backend, we used the FTS50 spectrometer, providing a bandwidth of 1820 MHz and a frequency resolution of 50 kHz. The latter corresponds to a velocity resolution of ~0.15 km s^{-1} at 86 GHz. The standard chopper wheel method was used to convert the observed signal to the antenna temperature $T_{\rm A}^*$ in units of K, corrected for the atmospheric attenuation. The data are given in terms of the main beam brightness temperature corresponding to $T_{\rm MB} = T_{\rm A}^* \times F_{\rm eff}/B_{\rm eff}$. During the observations, the system noise temperatures ranged from 80 K to 330 K. The telescope pointing was checked every hour by observing the quasar source 1741-038 and was found to be better than 3″ throughout the two runs. Our mapping observations were made with the on-the-fly (OTF) mapping technique. We chose the positions (RA$_{\rm J2000}$, Dec$_{\rm J2000}$) = (16:29:06.4, −24:26:57.0), (16:25:34.5, −24:36:44.0), and (16:26:14.5, −24:02:00.0) as our reference (off) positions. We decomposed the target field into a series of 10′ × 10′ subfields and took pairs of OTF maps toward each subfield using two perpendicular scanning directions (along the RA or Dec axes). Combining such pairs of OTF maps reduces scanning artifacts. We smoothed the data spatially with a Gaussian function resulting in an effective beam size of 40″. The 1σ noise level of the final mosaiced data cube at an effective angular resolution of 40″ and a velocity resolution of ~0.15 km s^{-1} is 0.07 K in $T_{\rm MB}$.

2.2. MOPRA observations toward the Ophiuchus cloud

Between 26 July 2015 and 2 August 2015, we carried out mapping observations toward a 0.21 deg^2 region in the Ophiuchus cloud, including the two subregions Oph/main (L1688) and Oph/cold (see Fig. A.2), with the 3 mm receiver installed on the MOPRA-22 m telescope. All molecular line data were obtained simultaneously. At 86 GHz, the telescope has a beam size of 39″ (HPBW) and a main beam efficiency $\eta_{\rm MB}$ of 49% (Ladd et al. 2005). As backend, we used the Mopra spectrometer (MOPS) in zoom mode, providing a bandwidth of 137.5 MHz and a frequency resolution of 33.8 kHz. The latter corresponds to a velocity resolution of ~0.1 km s^{-1} at 86 GHz. The standard chopper wheel method was used to convert the observed signal to the antenna temperature $T_{\rm A}^*$ in units of K, corrected for atmospheric attenuation. The data are given in main beam brightness temperature, $T_{\rm MB} = T_{\rm A}^*/\eta_{\rm MB}$. During the observations, the system noise temperatures ranged from 240 K to 420 K. The telescope pointing was checked every hour by observing the SiO maser sources AH Sco, VX Sgr, and W Hya, and was better than 5″ throughout the entire run. Our mapping observations were made with the OTF mapping technique. The positions (RA$_{\rm J2000}$, Dec$_{\rm J2000}$) = (16:29:06.4, −24:26:57.0), (16:25:34.5, −24:36:44.0), and (16:26:14.5, −24:02:00.0) were used as off positions. We obtained a series of OTF maps with two different scanning directions along the RA or Dec axes covering a subfield of 6′ × 6′ each and combined them into a single map to reduce scanning effects as much as possible. We smoothed the data spatially with a Gaussian function of 19.5″ (FWHM), resulting in an effective beam size of 50″. The scanning effects were minimized by combining scans along the RA and Dec directions with the Emerson & Graeve (1988) PLAIT algorithm. The 1σ noise level of the final data at an effective angular resolution of 50″ and a velocity resolution of 0.1 km s^{-1} is 0.5 K in $T_{\rm MB}$.

2.3. NRO 45 m observations toward the Orion B cloud

Between 7 May and 21 May 2015, we carried out mapping observations toward a 0.14 deg^2 region in the Orion B cloud, including the four subregions NGC 2023, NGC 2024, NGC 2068, and NGC 2071 (see Figs. A.3–A.6), with the TZ receiver on the Nobeyama 45 m telescope. All molecular line data were obtained simultaneously. At 86 GHz, the telescope has a beam size of 19.1″ (HPBW) and a main beam efficiency $\eta_{\rm MB}$ of ~50%. As backend, we used the SAM45 spectrometer which provides a bandwidth of 31 MHz and a frequency resolution of 7.63 kHz. The latter corresponds to a velocity resolution of ~0.02 km s^{-1} at 86 GHz. The standard chopper wheel method was used to convert the observed signal to the antenna temperature $T_{\rm A}^*$ in units of K, corrected for the atmospheric attenuation. The data are given in terms of the main beam brightness temperature, $T_{\rm MB} = T_{\rm A}^*/\eta_{\rm MB}$. During the observations, the system noise

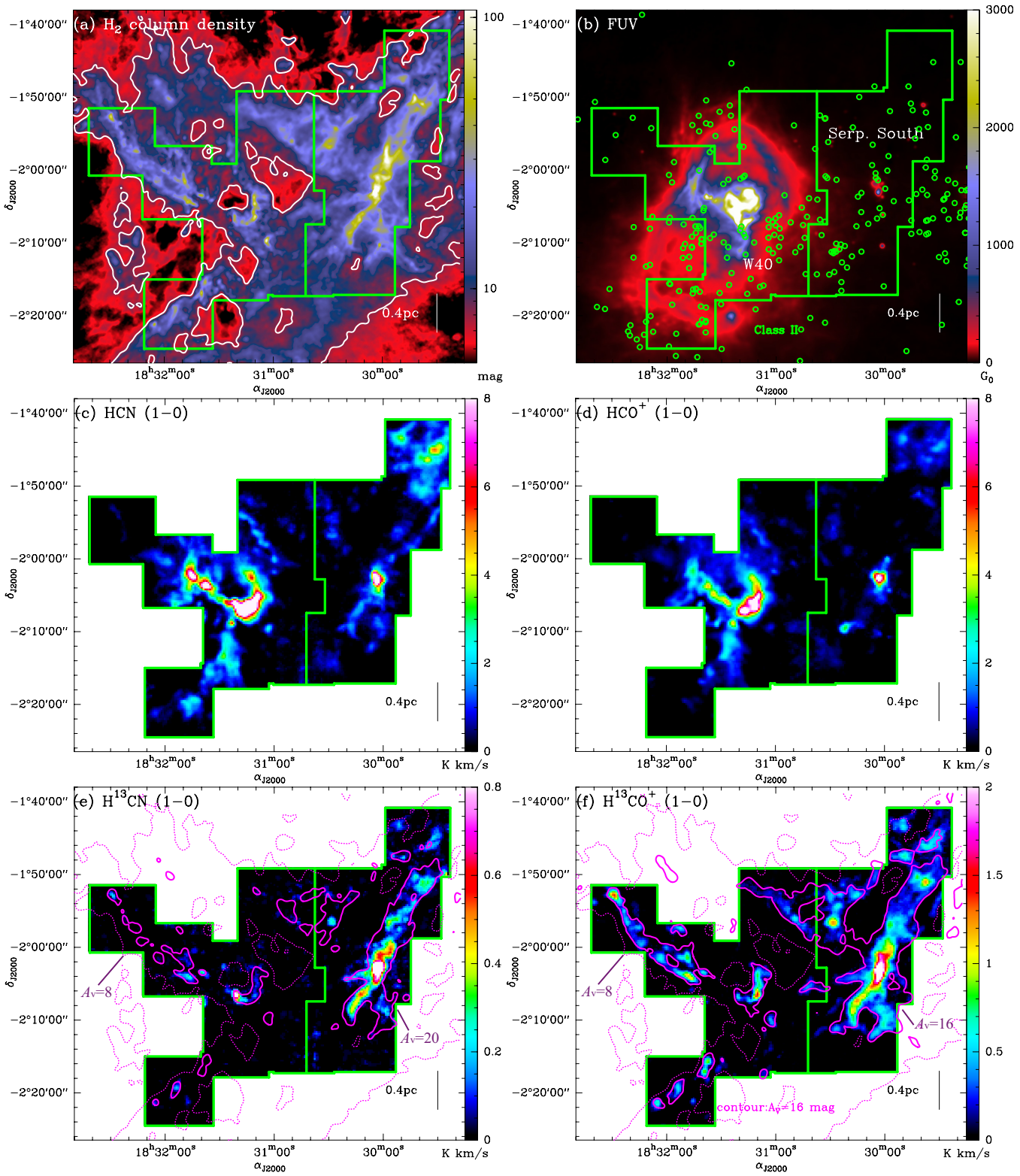

Fig. 1. *a)* Column density map of the Aquila region derived from *Herschel* Gould Belt survey (HGBS) data (André et al. 2010; Könyves et al. 2015) at an angular resolution of 18.2″ and in units of A_V. *b)* FUV field strength map derived from HGBS 70 μm and 100 μm data smoothed to an angular resolution of 18.2″ in Habing units, and integrated intensity maps of *c)* HCN(1–0); *d)* HCO^+(1–0); *e)* $H^{13}CN$(1–0); *f)* $H^{13}CO^+$(1–0) in units of K km s^{-1} (T_{MB}). The angular resolutions of the HCN, HCO^+, $H^{13}CN$, and $H^{13}CO^+$ maps are 40″, 40″, 40″, and 50″, respectively. In each panel, a green polygon outlines the field observed in molecular lines. The HCN and $H^{13}CN$ integrated intensity includes all components of the hyperfine structure (HFS). The white contour in *panel a* and the magenta dotted contours in *panels e* and *f* show the A_V = 8 level obtained after smoothing the *Herschel* column density map to 40″ resolution. In *panel b*, green open circles indicate the positions of the Class II objects identified by Dunham et al. (2015). In *panels e* and *f*, the magenta solid contour indicates the rough A_V column density level above which significant line emission is detected, i.e., A_V = 20 for $H^{13}CN$ (1–0) and A_V = 16 for $H^{13}CO^+$ (1–0).

Table 2. Physical parameters derived from $H^{13}CO^+$ (1–0) observations.

Region	$V_{\rm peak}$ [km s^{-1}]			d$V_{\rm FWHM}$ [km s^{-1}]			$N_{\rm H^{13}CO^+}$ [cm^{-2}]			$X_{\rm H^{13}CO^+}$		
	min	max	mean	min	max	mean	min	max	mean	min	max	mean
Aquila/W40	4.0	8.8	7.0	0.3	3.3	0.7	4.4×10^{10}	1.7×10^{12}	2.9×10^{10}	2.8×10^{-12}	1.2×10^{-11}	5.5×10^{-11}
Aquila/Serp S	3.8	8.9	7.3	0.3	2.3	0.8	4.6×10^{10}	4.1×10^{12}	3.3×10^{10}	3.3×10^{-12}	4.6×10^{-11}	1.5×10^{-11}
Aquila/cold	5.6	8.6	6.5	0.3	1.1	0.5	7.2×10^{10}	5.7×10^{11}	2.4×10^{11}	9.2×10^{-12}	4.1×10^{-11}	2.2×10^{-11}
Oph/main (L1688)	2.5	4.9	3.6	0.3	2.0	0.7	6.4×10^{11}	2.9×10^{12}	1.1×10^{12}	8.0×10^{-12}	2.0×10^{-10}	3.3×10^{-11}
Oph/cold	2.9	3.6	3.3	0.3	0.7	0.4	6.3×10^{11}	1.5×10^{12}	9.6×10^{11}	2.2×10^{-11}	1.2×10^{-10}	5.5×10^{-11}
Orion B/NGC 2023	8.1	11.7	10.0	0.2	2.3	1.0	2.6×10^{11}	37.8×10^{11}	15.2×10^{11}	1.8×10^{-11}	9.0×10^{-11}	5.0×10^{-11}
Orion B/NGC 2024	5.1	13.2	10.9	0.2	2.7	0.9	2.3×10^{11}	37.9×10^{11}	14.3×10^{11}	1.9×10^{-11}	9.7×10^{-11}	5.8×10^{-11}
Orion B/NGC 2068	7.1	14.8	10.9	0.2	1.8	0.6	2.3×10^{11}	22.4×10^{11}	10.2×10^{11}	1.8×10^{-11}	6.9×10^{-11}	4.5×10^{-11}
Orion B/NGC 2071	6.1	12.7	9.5	0.2	2.2	0.9	2.6×10^{11}	42.0×10^{11}	15.6×10^{11}	1.8×10^{-11}	1.1×10^{-10}	4.5×10^{-11}

temperatures ranged from 140 K to 630 K. The telescope pointing was checked every hour by observing the SiO maser source Ori-KL, and was better than 3″ throughout the entire observing run. Our mapping observations were made with the OTF mapping technique. We chose the positions (RA_{J2000}, Dec_{J2000}) = (5:39:21.819, −2:9:8.54) and (5:44:41.15, 0:33:4.98) as off positions. We obtained OTF maps with two different scanning directions along the RA or Dec axes covering a subfield of 6′ × 6′ and combined them into a single map to reduce the scanning effects as much as possible. As a convolution function, we adopted a Gaussian function with a FWHM of half the beam size. The scanning effects were minimized by combining scans along the RA and Dec directions with the Emerson & Graeve (1988) PLAIT algorithm. We also applied spatial smoothing to the data with a Gaussian function resulting in an effective beam size of 30″. The 1σ noise level of the final data at an effective resolution of 30″ and a velocity resolution of 0.1 km s^{-1} is 0.28 K in $T_{\rm MB}$.

3. Results and analysis

3.1. $H^{13}CO^+$(1–0) and $H^{13}CN$(1–0) emission

Figures 1 and A.1–A.6 compare the $H^{13}CO^+$(1–0), and $H^{13}CN$(1–0) integrated intensity maps observed toward Aquila, Ophiuchus, Orion B/NGC 2023, Orion B/NGC 2024, Orion B/NGC 2068, and Orion B/NGC 2071 with the column density maps derived from HGBS data toward the same sub-regions. Above the $A_{\rm V}$ = 16 contour in the *Herschel* column density maps (assuming $N_{\rm H_2}/A_{\rm V} = 0.94\times10^{21}$ cm^{-2}, Bohlin et al. 1978), it can be seen that the spatial distribution of the $H^{13}CO^+$(1–0) emission is closely correlated with the texture of the dense gas (e.g., filamentary structure) seen by *Herschel*. In particular, the $H^{13}CO^+$(1–0) emission traces the dense "supercritical" filaments detected by *Herschel* very well. Likewise, the spatial distribution of the $H^{13}CN$ (1–0) emission is closely correlated with the column density distribution above the $A_{\rm V}$ = 20 level, especially in the Aquila and Orion B/NGC 2024 regions. As apparent in Figs. 1 and A.1–A.6, and in agreement with the effective excitation densities quoted in Sect. 2, the $H^{13}CN$ (1–0) emission traces higher column density gas compared to the $H^{13}CO^+$ (1–0) emission. Figure A.7 displays mean $H^{13}CN$(1–0) spectra, obtained by averaging the data over the detected portion of each region and sub-region.

The 1 K km s^{-1} level in the $H^{13}CO^+$(1–0) integrated intensity map roughly matches the $A_{\rm V}$ = 30 level in the *Herschel* column density map (see Fig. 1f), which in turn corresponds to a volume density ~8.6×10^4 cm^{-3} assuming most of the dense gas is concentrated in ~0.1 pc filaments (cf. Sect. 1). This is roughly consistent with the $H^{13}CO^+$ (1–0) effective excitation density of ~4×10^4 cm^{-3}, suggesting that local thermodynamical equilibrium (LTE) may not be too bad an approximation for $H^{13}CO^+$(1–0). Under the LTE assumption, the column density of $H^{13}CO^+$ can be derived as follows (cf. Tsuboi et al. 2011):

$$N_{\rm H^{13}CO^+}\left[{\rm cm^{-2}}\right] = 5.99\times10^{10} T_{\rm ex}\int T_{\rm MB}{\rm d}v\ [{\rm K\,km\,s^{-1}}]. \quad (1)$$

We further assume that the excitation temperature $T_{\rm ex}$ of the $H^{13}CO^+$ (1–0) transition is equal to the dust temperature $T_{\rm dust}$ derived from the HGBS data. The dust temperature ranges from 11 K to 46 K. Table 2 summarizes the results. The mean $H^{13}CO^+$ column densities range from 2.9×10^{10} cm^{-2} to 1.6×10^{12} cm^{-2}. The $H^{13}CO^+$ abundances relative to H_2, $X_{\rm H^{13}CO^+} \equiv N_{\rm H^{13}CO^+}/N_{\rm H_2}$, have mean values in the range (1.5–5.8) × 10^{-11}, using $N_{\rm H^{13}CO^+}$ values estimated from the present data and $N_{\rm H_2}$ values from HGBS data (André et al. 2010; Könyves et al. 2015). These abundance estimates are consistent within a factor of a few with the findings of previous studies in other regions ($1.1\pm0.1\times10^{-11}$ in OMC2-FIR4: Shimajiri et al. 2015b; and $1.8\pm0.4\times10^{-11}$ in Sagittarius A: Tsuboi et al. 2011).

Assuming spherical shapes and uniform density, the virial masses $M^{\rm detect}_{\rm VIR,mol}$ of the detected clumps and structures can be estimated as (see Ikeda et al. 2007; Shimajiri et al. 2015a),

$$M^{\rm detect}_{\rm VIR,mol}\,[M_\odot] = \frac{5R^{\rm detect}_{\rm mol}\sigma^2}{G} = 209\left(\frac{R^{\rm detect}_{\rm mol}}{\rm pc}\right)\left(\frac{{\rm d}V^{\rm detect}_{\rm mol}}{\rm km\,s^{-1}}\right)^2. \quad (2)$$

The radius $R^{\rm detect}_{\rm mol}$ of each clump or cloud was estimated as $R^{\rm detect}_{\rm mol}$ [pc] = $\sqrt{A^{\rm detect}_{\rm mol}/\pi}$. The velocity dispersion σ was determined as $\sigma = {\rm d}V^{\rm detect}_{\rm mol}/\sqrt{8\ln 2}$, where ${\rm d}V^{\rm detect}_{\rm mol}$ is the mean FWHM velocity width among pixels where the emission was detected. The derived values ${\rm d}V^{\rm detect}_{\rm mol}$, $R^{\rm detect}_{\rm mol}$, $A^{\rm detect}_{\rm mol}$, and $M^{\rm detect}_{\rm VIR,mol}$ are given in Tables 3 and 4.

We also estimated the total virial mass $M^{A_{\rm V}>8}_{\rm VIR,mol}$ of the area above $A_{\rm V}$ = 8 for each cloud by scaling the virial mass derived for the detected subregion using the well-known linewidth-size relation $\sigma_V \propto L^{0.5}$ (Larson 1981; Heyer et al. 2009). In practice, we assumed

$${\rm d}V^{A_{\rm V}>8}_{\rm mol}\left[{\rm km\,s^{-1}}\right] = {\rm d}V^{\rm detect}_{\rm mol}\left(\frac{R^{A_{\rm V}>8}_{Herschel}}{R^{\rm detect}_{\rm mol}}\right)^{0.5}, \quad (3)$$

and we estimated the cloud radius $R^{A_{\rm V}>8}_{Herschel}$ as $R^{A_{\rm V}>8}_{Herschel}$ [pc] = $\sqrt{A^{A_{\rm V}>8}_{Herschel}/\pi}$, where $A^{A_{\rm V}>8}_{Herschel}$ is the projected area of each observed cloud above $A_{\rm V}$ = 8. The total virial mass, $M^{A_{\rm V}>8}_{\rm VIR,H^{13}CO^+}$,

Table 3. Virial masses from $H^{13}CO^{+\dagger}$.

Region	$dV^{detect}_{H^{13}CO^+}$ [km s^{-1}]	$A^{detect}_{H^{13}CO^+}$ [pc^2]	$R^{detect}_{H^{13}CO^+}$ [pc]	$M^{detect}_{VIR,H^{13}CO^+}$ [$M_\odot$]	$M^{H^{13}CO^+-detect}_{Herschel}$ [$M_\odot$]	$\frac{M^{detect}_{VIR,H^{13}CO^+}}{M^{H^{13}CO^+-detect}_{Herschel}}$	$dV^{A_V>8}_{H^{13}CO^+}$ [km s^{-1}]	$A^{A_V>8}_{H^{13}CO^+}$ [pc^2]	$R^{A_V>8}_{H^{13}CO^+}$ [pc]	$M^{A_V>8}_{VIR,H^{13}CO^+}$ [$M_\odot$]	$M^{A_V>8}_{Herschel}$ [$M_\odot$]	$\frac{M^{A_V>8}_{VIR,H^{13}CO^+}}{M^{A_V>8}_{Herschel}}$
Aquila/W40	1.66	0.90	0.54	307.3	339.1	0.9	2.18	2.68	0.92	917.0	748.1	1.2
Aquila/Serp S	1.19	1.53	0.70	205.8	707.4	0.3	1.35	2.51	0.89	339.0	954.1	0.4
Aquila/cold	1.04	0.36	0.34	76.7	74.2	1.0	1.07	0.40	0.36	85.9	88.8	1.0
Aquila (total)	–	–	–	589.8	1120.8	0.5	–	–	–	1341.8	1790.9	0.7
Oph/main (L1688)	1.48	0.23	0.27	122.0	167.9	0.7	2.09	0.91	0.54	492.0	416.0	1.2
Oph/cold	0.40	0.02	0.07	2.5	6.5	0.4	0.55	0.06	0.14	8.5	16.2	0.5
Oph (total)	–	–	–	124.5	174.4	0.7	–	–	–	500.5	432.1	1.2
Orion B/NGC2023	1.50	0.30	0.31	144.9	175.2	0.8	1.89	0.76	0.49	367.7	300.1	1.2
Orion B/NGC2024	1.97	0.26	0.29	236.3	206.3	1.1	2.57	0.76	0.49	680.8	335.2	2.0
Orion B/NGC2068	0.99	0.23	0.27	55.0	113.7	0.5	1.21	0.52	0.41	125.3	189.6	0.7
Orion B/NGC2071	1.23	0.46	0.38	121.1	262.9	0.5	1.47	0.94	0.55	247.3	398.7	0.6
Orion B (total)	–	–	–	557.3	758.2	0.7	–	–	–	1421.1	1223.5	1.2

Notes. [†] See Table A.2 for the definition of each notation.

Table 4. Virial masses from $H^{13}CN^{\dagger}$.

Region	$dV^{detect}_{H^{13}CN}$ [km s^{-1}]	$A^{detect}_{H^{13}CN}$ [pc^2]	$R^{detect}_{H^{13}CN}$ [pc]	$M^{detect}_{VIR,H^{13}CN}$ [$M_\odot$]	$M^{H^{13}CN-detect}_{Herschel}$ [$M_\odot$]	$\frac{M^{detect}_{VIR,H^{13}CN}}{M^{H^{13}CN-detect}_{Herschel}}$	$dV^{A_V>8}_{H^{13}CN}$ [km s^{-1}]	$A^{A_V>8}_{Herschel}$ [pc^2]	$R^{A_V>8}_{Herschel}$ [pc]	$M^{A_V>8}_{VIR,H^{13}CN}$ [$M_\odot$]	$M^{A_V>8}_{Herschel}$ [$M_\odot$]	$\frac{M^{A_V>8}_{VIR,H^{13}CN}}{M^{A_V>8}_{Herschel}}$
Aquila/W40	1.40	0.25	0.28	115.0	108.5	1.1	2.54	2.68	0.92	1246.8	748.1	1.7
Aquila/Serp S	1.17	0.77	0.49	140.7	445.0	0.3	1.57	2.51	0.89	460.6	954.1	0.5
Oph/main(L1688)	1.58	0.16	0.23	117.2	90.0	1.3	2.43	0.91	0.54	665.5	416.0	1.6
Orion B/NGC2024	1.86	0.20	0.25	181.5	172.2	1.1	2.62	0.76	0.49	705.5	335.2	2.1
Orion B/NGC2068	1.91	0.17	0.23	179.0	71.8	2.5	2.53	0.52	0.41	546.4	189.6	2.9
Orion B/NGC2071	1.90	0.37	0.34	257.1	203.0	1.3	2.40	0.94	0.55	661.7	398.7	1.7

Notes. [†] See Table A.2 for the definition of each notation.

was then estimated from the scaled velocity width ($dV^{A_V>8}_{VIR,mol}$) using Eq. (2).

The mass of each cloud was also estimated from HGBS data as

$$M_X\,[M_\odot] = \Sigma_{Herschel} A_Y, \tag{4}$$

$$\Sigma_{Herschel} = N(H_2)\, m_H \mu_{H_2}, \tag{5}$$

where M_X (either $M^{mol-detect}_{Herschel}$ or $M^{A_V>8}_{Herschel}$) is the mass integrated over the area of the corresponding *Herschel* column density map where ($H^{13}CO^+$ or $H^{13}CN$) line emission was detected or where $A_V > 8$. A_Y is the surface area (either A^{detect}_{mol} or $A^{A_V>8}_{Herschel}$), m_H is the hydrogen atom mass, and $\mu_{H_2} = 2.8$ is the mean molecular weight per H_2 molecule. The uncertainties in $M^{mol-detect}_{Herschel}$ and $M^{A_V>8}_{Herschel}$ are typically a factor 2, mainly due to uncertainties in the dust opacity (cf. Roy et al. 2014). The total gas masses derived from *Herschel*, $M^{H^{13}CO^+-detect}_{Herschel}$ and $M^{A_V>8}_{Herschel}$, range from 6.5 $M_\odot$ to 707 $M_\odot$ and from 16 $M_\odot$ to 954 $M_\odot$, respectively.

Tables 3 and 4 also include estimates of the virial mass ratios, $\mathcal{R}^{detect}_{VIR,mol}$ and $\mathcal{R}^{A_V>8}_{VIR,mol}$, defined as

$$\mathcal{R}^{detect}_{VIR,mol} = \frac{M^{detect}_{VIR,mol}}{M^{mol-detect}_{Herschel}}, \tag{6}$$

and

$$\mathcal{R}^{A_V>8}_{VIR,mol} = \frac{M^{A_V>8}_{VIR,mol}}{M^{A_V>8}_{Herschel}}. \tag{7}$$

The $\mathcal{R}^{detect}_{VIR,H^{13}CO^+}$ and $\mathcal{R}^{A_V>8}_{VIR,H^{13}CO^+}$ ratios range from ~0.30 to ~1.1 and from ~0.40 to ~2.0, respectively, suggesting that all the dense clumps we observed are gravitationally bound, especially the portions detected in $H^{13}CO^+$. Figure 2a plots $M^{A_V>8}_{VIR,H^{13}CO^+}$ against $M^{A_V>8}_{Herschel}$, and shows that these two estimates of the mass of dense ($A_V > 8$) gas agree to within better than 50% in each region (see also Table 3).

We also estimated $M^{detect}_{VIR,H^{13}CN}$ and $M^{A_V>8}_{VIR,H^{13}CN}$ for the regions where $H^{13}CN$ emission was detected, i.e., Aquila/W40, Aquila/Serp. South, Oph/main, Orion B/NGC 2024, Orion B/NGC 2068, and Orion B/NGC 2071. The virial mass ratios $\mathcal{R}^{detect}_{VIR,H^{13}CN}$ and $\mathcal{R}^{A_V>8}_{VIR,H^{13}CN}$ range from 0.3 to 2.5 and from 0.5 to 2.9, respectively (see also Fig. 2b).

3.2. HCN (1–0) & HCO^+ (1–0) emission

In contrast to the $H^{13}CO^+$ emission, the spatial distributions of HCN(1–0) and HCO^+(1–0) emission differ significantly from the column density distribution derived from *Herschel* data, as shown in Figs. 1 and A.1–A.6. The HCN(1–0) and HCO^+(1–0) maps appear to trace more extended regions than the denser filaments traced in the *Herschel* column density maps. In the Aquila cloud, the HCN(1–0) and HCO^+ (1–0) integrated intensities are strongest toward the W40 HII subregion, while column density is highest in the Serpens South subregion. The W40 HII region is known to be excited by the luminous stars IRS 1A North of spectral type O9.5 and IRS 1A South of spectral type B1V (Shuping et al. 2012). In the Ophiuchus cloud, the HCN(1–0) and HCO^+(1–0) integrated intensities tend to be strong around the compact HII region excited by the B3 star S1 (Grasdalen et al. 1973; André et al. 1988). These findings suggest that the HCN(1–0) and HCO^+(1–0) intensities depend on the strength of the local FUV radiation field.

Figure 3 shows comparisons of the mean $H^{13}CO^+$(1–0), HCO^+(1–0) and HCN(1–0) spectra observed toward each region. Clear dips in the HCN(1–0) and HCO^+(1–0) spectra can be seen at $V_{LSR} \sim 7, 4, 10$ km s^{-1} in Aquila/W40, Oph/main, and

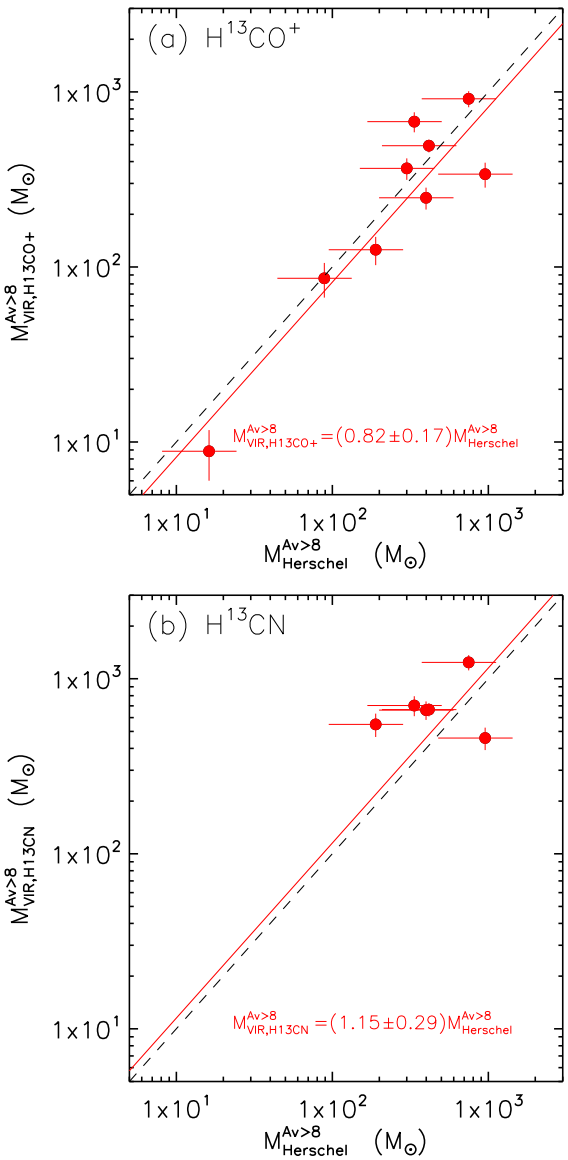

Fig. 2. *a)* $M^{A_V>8}_{\rm VIR,H^{13}CO^+}$ vs. $M^{A_V>8}_{Herschel}$ and *b)* $M^{A_V>8}_{\rm VIR,H^{13}CN}$ vs. $M^{A_V>8}_{Herschel}$ relations. The black dashed lines indicate $M^{A_V>8}_{\rm VIR,mol} = M^{A_V>8}_{Herschel}$ and the red lines indicate the best-fit results: $M^{A_V>8}_{\rm VIR,H^{13}CO^+} = (0.82 \pm 0.17) \times M^{A_V>8}_{Herschel}$ and $M^{A_V>8}_{\rm VIR,H^{13}CN} = (1.15 \pm 0.29) \times M^{A_V>8}_{Herschel}$. (The uncertainty in $M^{A_V>8}_{\rm VIR,mol}$ was derived from the uncertainties in $R^{A_V>8}_{Herschel}$ and in $dV^{A_V>8}_{\rm mol}$ (see Ikeda et al. 2007; Shimajiri et al. 2015a.) The *x*- and *y*-axis ranges are the same in both panels.

Orion B/NGC 2071, respectively. Furthermore, the velocities of these dips coincide with the peak velocities of the $H^{13}CO^+$(1–0) spectra. This suggests that the HCN(1–0) and HCO^+(1–0) spectra are strongly affected by self-absorption effects. In these subregions, the blueshifted components of the HCN(1–0) and HCO^+(1–0) spectra are stronger than the redshifted components. This type of asymmetric spectral shape, known as blue-skewed asymmetry, suggests the presence of infalling motions in the clouds (cf. Myers et al. 1996; Schneider et al. 2010). Thus, the Aquila/W40, Oph/main, and Orion B/NGC 2071 clumps may be undergoing large-scale collapse.

Assuming the same excitation temperature for the two isotopic species and a $^{12}C/^{13}C$ isotopic ratio $R_{\rm i} = 62$ (Langer & Penzias 1993), we also estimate the optical depth of

Table 5. HCN (1–0) to HCO^+ (1–0) line intensity ratios.

Region	Median	Standard deviation
Aquila	1.6	1.5
Oph	1.3	0.9
Orion B/NGC2023	0.7	0.2
Orion B/NGC2024	1.1	0.3
Orion B/NGC2068	1.0	0.3
Orion B/NGC2071	0.9	0.2

HCN(1–0) and HCO^+(1–0) as follows:

$$\frac{T_{\rm peak}(i)}{T_{\rm peak}(n)} = \frac{1 - {\rm e}^{-\tau(n)}/R_{\rm i}}{1 - {\rm e}^{-\tau(n)}}, \tag{8}$$

where $T_{\rm peak}(i)$ is the peak intensity of the rare isotopic species [$H^{13}CN$(1–0) or $H^{13}CO^+$(1–0)] derived from mean spectra averaged over the observed area (see Fig. 3), whereas $T_{\rm peak}(n)$ and $\tau(n)$ are the peak intensity and optical depth of the normal species [HCN(1–0) or HCO^+(1–0)] at the peak velocity of the rare isotopic species in the averaged spectra. In all observed regions, the HCN(1–0) and HCO^+(1–0) lines are optically thick (see also Table A.1).

Recently, Braine et al. (2017) observed a significant dependence of the $I_{\rm HCN}/I_{\rm HCO^+}$ intensity ratio on metallicity, with $I_{\rm HCN}/I_{\rm HCO^+}$ increasing from ~1/4 at 0.3 solar metallicity to ~1 at solar metallicity among galaxies of the local group. In the nearby clouds observed here, the median $I_{\rm HCN}/I_{\rm HCO^+}$ intensity ratio ranges from 0.7 to 1.6 (see Table 5), consistent with the solar or near solar metallicity of these clouds.

3.3. Estimating the strength of the FUV radiation field

The FUV field strength, G_0, can be derived from *Herschel* 70 μm and 100 μm photometric data using the following equations (Kramer et al. 2008; Schneider et al. 2016):

$$G_0 = \frac{4\pi I_{\rm FIR}}{1.6 \times 10^{-3}\ [{\rm erg\,cm^{-2}\,s^{-1}}]}\ [\text{in Habing units}] \tag{9}$$

$$I_{\rm FIR} = \left(\frac{F_{70\ \mu{\rm m}}}{[{\rm erg\,cm^{-2}\,s^{-1}\,Hz^{-1}\,sr^{-1}}]} \times \frac{B_{60\ \mu{\rm m}-80\ \mu{\rm m}}}{[{\rm Hz}]}\right) + \left(\frac{F_{100\ \mu{\rm m}}}{[{\rm erg\,cm^{-2}\,s^{-1}\,Hz^{-1}\,sr^{-1}}]} \times \frac{B_{80\ \mu{\rm m}-125\ \mu{\rm m}}}{[{\rm Hz}]}\right)[{\rm erg\,cm^{-2}\,s^{-1}\,sr^{-1}}], \tag{10}$$

where $I_{\rm FIR}$ is the far-infrared (FIR) intensity, and $B_{60\ \mu{\rm m}-80\ \mu{\rm m}}$ and $B_{80\ \mu{\rm m}-125\ \mu{\rm m}}$ are the bandwidths of the *Herschel*/PACS broad-band filters at 70 μm and 100 μm, respectively. The G_0 values are in units of the local interstellar radiation field (Habing 1968).

According to Hollenbach et al. (1991), G_0 can also be estimated from the dust temperature $T_{\rm dust}$ based on the following relations:

$$T_{\rm d} = \Big(8.9 \times 10^{-11} \nu_0 G_0 \exp\big(-1.8 A_{\rm V}\big) + 2.7^5 + 3.4 \times 10^{-2}\big[0.42 - \ln\big(3.5 \times 10^{-2} \tau_{100} T_0\big]\big)\tau_{100} T_0^6\Big)^{0.2}\ [{\rm K}] \tag{11}$$

$$T_0 = 12.2 G_0^{0.2}\ [{\rm K}] \tag{12}$$

$$\tau_{100} = \frac{2.7 \times 10^2}{T_0^5} G_0 \tag{13}$$

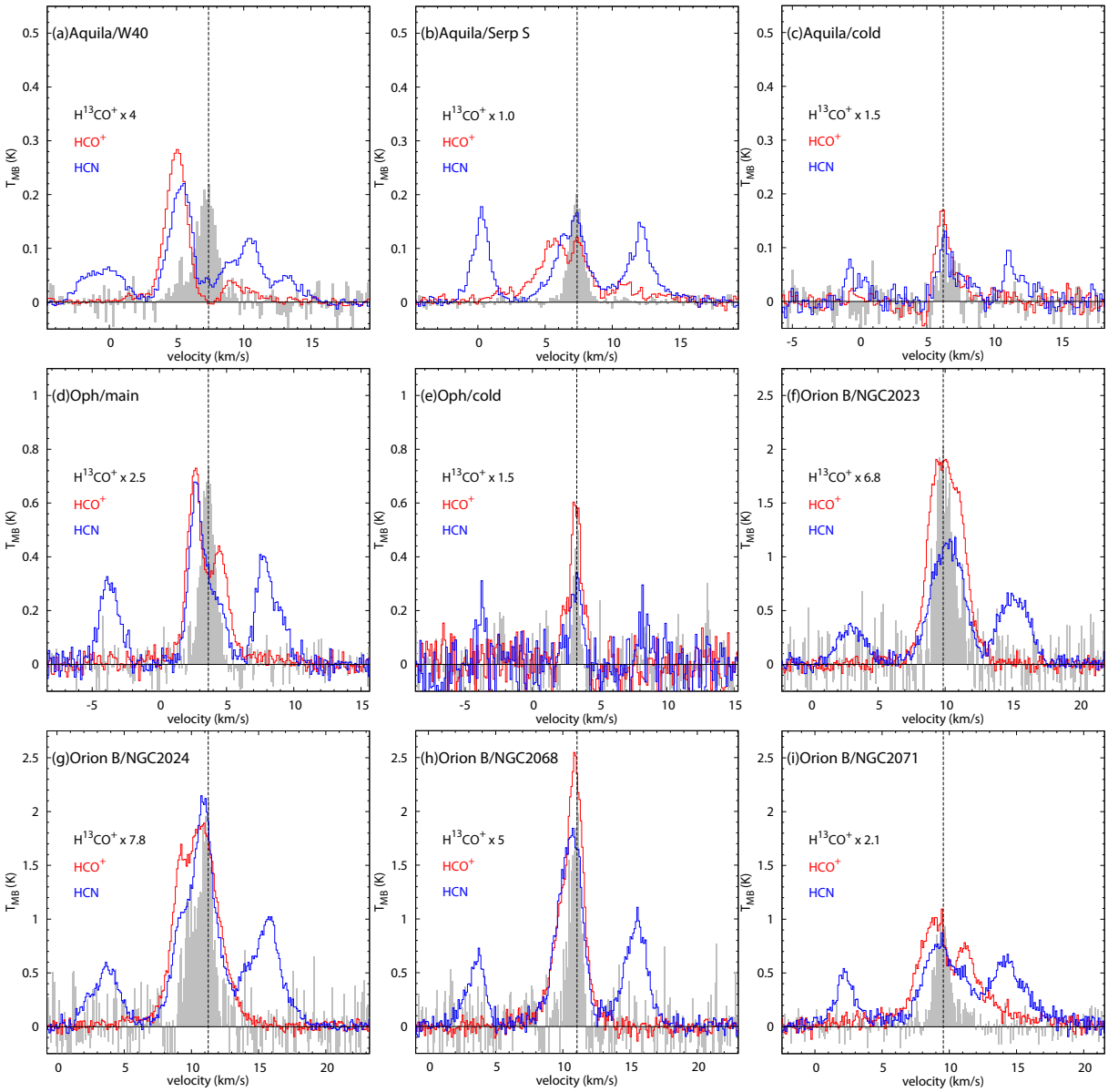

Fig. 3. Comparison of the HCN, HCO^+, and $H^{13}CO^+$(1–0) spectra averaged over the observed area in *a)* Aquila/W40; *b)* Aquila/Serp–South; *c)* Aquila/cold; *d)* Oph/main; *e)* Oph/cold; *f)* Orion B/NGC 2023; *g)* Orion B/NGC 2024; *h)* Orion B/NGC 2068; and *i)* Orion B/NGC 2071. In each panel, blue, red, and gray lines show the mean HCN, HCO^+, and $H^{13}CO^+$(1–0) spectra in the corresponding subregion; the vertical dashed line marks the peak velocity of the $H^{13}CO^+$(1–0) line.

where, τ_{100}, T_0, and ν_0 are the effective optical depth at 100 μm, the dust temperature of the cloud surface, and the frequency at 0.1 μm.

Figure A.8 shows the pixel-to-pixel correlation between the G_0 values estimated in our target clouds from *Herschel* 70 μm and 100 μm data using Eqs. ((9), (10)) and the G_0 values estimated from the *Herschel* $T_{\rm dust}$ maps using Eqs. ((11)–(13)). The best-fit results are $G_0(T_{\rm dust}) = 1.38 \times G_0(70, 100\,\mu{\rm m})$ for Aquila, $G_0(T_{\rm dust}) = 0.62 \times G_0(70, 100\,\mu{\rm m})$ for Oph, and $G_0(T_{\rm dust}) = 2.60 \times G_0(70, 100\,\mu{\rm m})$ for Orion B. In Orion B, the highest G_0 values come from pixels in NGC 2024 and affect the best-fit results. The best-fit results for pixels with $G_0(70, 100\,\mu{\rm m}) < 100$ is $G_0(T_{\rm dust}) = 1.04 \times G_0(70, 100\,\mu{\rm m})$. In summary, our two estimates of G_0 generally agree to within a factor 2 to 3. Pety et al. (2017) also estimated the strength of the FUV radiation field toward NGC 2023/2024 in Orion B using Eq. (12). Their estimate agrees with our $G_0(70, 100\,\mu{\rm m})$ value within 30%.

4. Discussion

4.1. Evidence of large variations in the α_{HCN} and α_{HCO^+} conversion factors

In many extragalactic studies (e.g., Gao & Solomon 2004a), the mass of dense gas $M_{\rm dense}$ is estimated from the HCN(1–0) luminosity $L_{\rm HCN}$ using the relation $M_{\rm dense} = \alpha_{\rm HCN} L_{\rm HCN}$ and assuming a fixed conversion factor $\alpha_{\rm HCN}$. Gao & Solomon derived a simple formula for the conversion factor, namely $\alpha_{\rm GS04-HCN} = 2.1\sqrt{n({\rm H_2})}/T_{\rm b} = 10\ M_\odot\ ({\rm K\,km\,s^{-1}\,pc^2})^{-1}$, under the assumption that the HCN(1–0) emission originates from gravitationally-bound "cores" or clumps with volume-averaged density $n({\rm H_2}) \sim 3 \times 10^4$ cm^{-3} and brightness temperature $T_{\rm b} \sim 35$ K. On this basis, they adopted the single value $\alpha_{\rm GS04-HCN} = 10\ M_\odot\ ({\rm K\,km\,s^{-1}\,pc^2})^{-1}$ in their seminal HCN study of galaxies (Gao & Solomon 2004a). Clearly, however,

Table 6. Derived parameters for the dense portions of the target nearby clouds where $A_{\rm V}$ > 8 mag.

Region	$M_{Herschel}^{\rm map>8\ mag\dagger}$ [$M_\odot$]	G_0	$A_{Herschel}^{\rm map>8\ mag\dagger}$ [pc^2]	$I_{\rm HCN}$ [K km s^{-1}]	$L_{\rm HCN}$ [K km s^{-1} pc^2]	$\alpha_{Herschel-{\rm HCN}}{}^{\dagger}$ [$M_\odot$ (K km s^{-1} pc^2)$^{-1}$]	$I_{\rm HCO^+}$ [K km s^{-1}]	$L_{\rm HCO^+}$ [K km s^{-1} pc^2]	$\alpha_{Herschel-{\rm HCO^+}}{}^{\dagger}$ [$M_\odot$ (K km s^{-1} pc^2)$^{-1}$]
Aquila/W40	748	327	2.68	1.13	3.04	246	0.75	2.01	372
Aquila/Serp S	954	20	2.51	0.91	2.30	416	0.60	1.52	629
Aquila/cold	89	1	0.40	0.48	0.20	454	0.33	0.13	667
Oph/main (L1688)	416	134	0.91	2.68	2.44	170	1.90	1.73	241
Oph/cold	16	5	0.06	0.79	0.05	354	0.73	0.04	386
Orion B/NGC2023	300	226	0.76	7.21	5.49	55	7.53	5.74	52
Orion B/NGC2024	335	4091	0.76	12.57	9.59	35	8.72	6.65	50
Orion B/NGC2068	190	134	0.52	8.32	4.36	44	5.54	2.90	65
Orion B/NGC2071	399	121	0.94	6.79	6.41	62	5.62	5.31	75

Notes. [(†)] See Table A.2 for the definition of each notation.

if the brightness temperature of the HCN emitting clumps is larger than 35 K or if their volume-averaged density is less than 3×10^4 cm^{-3}, the $\alpha_{\rm GS04-HCN}$ factor can become smaller than 10 $M_\odot$ (K km s^{-1} pc^2)$^{-1}$. Calibrating the conversion factor $\alpha_{\rm HCN}$ in Galactic clouds and assessing its potential variations is thus of crucial importance. For a sample of massive Galactic clumps, Wu et al. (2005) investigated the relationship between virial mass (estimated from $C^{34}S$ observations) and HCN luminosity and found a logarithmic mean value $\alpha_{\rm Wu05-HCN}$ = 7 ± 2 $M_\odot$ (K km s^{-1} pc^2)$^{-1}$ for the conversion factor. The fact that the $\alpha_{\rm Wu05-HCN}$ and $\alpha_{\rm GS04-HCN}$ values differ by only ~30% is very encouraging for extragalactic studies, but the HCN excitation conditions in the massive clumps studied by Wu et al. (2005) are not necessarily representative of the bulk of the HCN-emitting dense gas in galaxies.

Here, we have both high-resolution HCN data and independent estimates of the mass of dense gas (from *Herschel* data) for a sample of nearby clouds/clumps spanning a broad range of radiation-field conditions, and are thus in a good position to calibrate the $\alpha_{\rm HCN}$ factor. To do so, we used the mass estimates derived from the *Herschel* column density maps, $M_{Herschel}^{A_{\rm V}>8}$, and the HCN(1–0) luminosities from the present observations to compute a $\alpha_{Herschel-{\rm HCN}} \equiv M_{Herschel}^{A_{\rm V}>8}/L_{\rm HCN}$ factor for each cloud in our sample. As explained in Sect. 1, because most of the dense gas is distributed in filaments of ~0.1 pc width, the $A_{\rm V}$ > 8 level in *Herschel* column density maps of nearby molecular clouds is an excellent tracer of the gas denser than $n_{\rm H_2} \sim 2.3 \times 10^4$ cm^{-3}, corresponding to supercritical, star-forming filaments (cf. André et al. 2014). The H_2 volume density of 2×10^4 cm^{-3} is also very close to the typical gas density of $\gtrsim 3 \times 10^4/\tau$ cm^{-3} traced by the HCN(1–0) line in normal spiral galaxies (Gao & Solomon 2004a, where $\tau \gtrsim 1$ is the optical depth of the line) and lies between the effective excitation density (8.4×10^3 cm^{-3}) and the critical density ($\gtrsim 3 \times 10^5$ cm^{-3}) of HCN(1–0) (Shirley 2015). The masses $M_{Herschel}^{A_{\rm V}>8}$ derived from *Herschel* data therefore provide good reference estimates of the mass of dense gas in nearby clouds. The estimated values of $\alpha_{Herschel-{\rm HCN}}$ range from ~35 to ~454 $M_\odot$ (K km s^{-1} pc^2)$^{-1}$ (see Table 6). Clearly, large variations in $\alpha_{Herschel-{\rm HCN}}$ are present.

As described in Sect. 3.2, the HCN emission tends to be strong in areas where the FUV radiation field is strong. Meijerink et al. (2007) demonstrated that the HCN emission is stronger in photon-dominated regions (PDRs) by a factor of two for densities larger than 10^5 cm^{-3}. Therefore, the variations we observe in $\alpha_{Herschel-{\rm HCN}}$ may be due to variations in the strength of the FUV field among the sub-regions.

The blue filled circles in Fig. 4 show a correlation plot between $\alpha_{Herschel-{\rm HCN}}$ and the mean FUV radiation field strength, G_0, estimated from *Herschel* 70 μm and 100 μm data (cf. Sect. 3.3). The correlation coefficient between the two variables

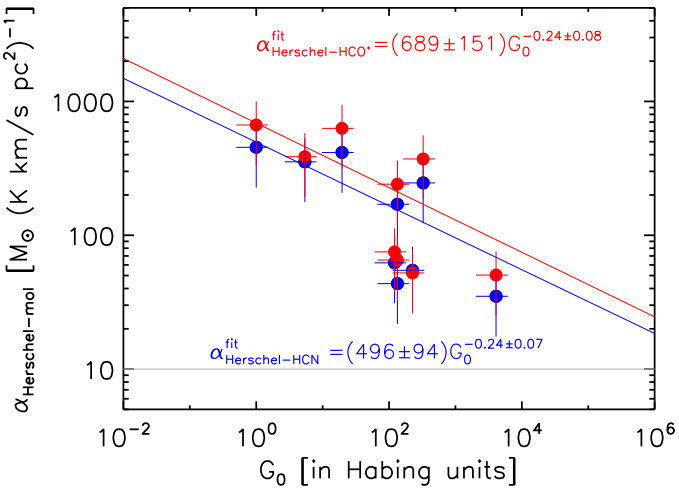

Fig. 4. Correlations between $\alpha_{Herschel-{\rm HCN}}$ and G_0 (blue line and filled circles) and between $\alpha_{Herschel-{\rm HCO^+}}$ and G_0 (red line and filled circles). The blue and red lines correspond to the best-fit relations: $\alpha^{\rm fit}_{Herschel-{\rm HCN}} = (496 \pm 94) \times G_0^{-0.24\pm0.07}$ [$M_\odot$ (K km s^{-1} pc^2)$^{-1}$] and $\alpha^{\rm fit}_{Herschel-{\rm HCO^+}} = (689 \pm 151) \times G_0^{-0.24\pm0.08}$ [$M_\odot$ (K km s^{-1} pc^2)$^{-1}$]. The horizontal line marks $\alpha_{\rm GS04-HCN}$ = 10 [$M_\odot$ (K km s^{-1} pc^2)$^{-1}$]. The uncertainties in $\alpha_{Herschel-{\rm HCN}}$ and $\alpha_{Herschel-{\rm HCO^+}}$ as estimated from the $M_{Herschel}^{A_{\rm V}>8}$ uncertainties are a factor of 2 (Roy et al. 2014). The uncertainties in G_0 are also a factor of 2 (see Sect. 3.3).

is −0.82, showing the presence of a clear anti-correlation. Quantitatively, $\alpha_{Herschel-{\rm HCN}}$ decreases as G_0 increases according to the following empirical relation:

$$\alpha^{\rm fit}_{Herschel-{\rm HCN}} = (496 \pm 94) \times G_0^{-0.24\pm0.07} \left[M_\odot \left({\rm K\,km\,s^{-1}\,pc^2}\right)^{-1}\right]. \quad (14)$$

Figure 5a plots the mass of dense gas $M_{\rm dense,HCN}$ estimated from HCN for each cloud in our sample, using both the standard extragalactic conversion factor $\alpha_{\rm GS04-HCN}$ [=10 (K km s^{-1} pc^2)$^{-1}$] (black open squares) and the conversion factor $\alpha^{\rm fit}_{Herschel-{\rm HCN}}$ from Eq. (14) (red filled circles), as a function of the reference mass estimate $M_{Herschel}^{A_{\rm V}>8}$. As can be seen, the $M_{\rm dense,HCN}$ values obtained with the $\alpha_{\rm GS04-HCN}$ conversion factor underestimate the reference masses $M_{Herschel}^{A_{\rm V}>8}$ by an order of magnitude on average in nearby clouds. In contrast, the $M_{\rm dense,HCN}$ estimates using the G_0-dependent conversion factor $\alpha^{\rm fit}_{Herschel-{\rm HCN}}$ agree well with the reference dense gas mass estimates $M_{Herschel}^{A_{\rm V}>8}$.

The HCO^+(1–0) line is another tracer of dense gas which can be used in extragalactic studies (Braine et al. 2017). Like the HCN emission, the HCO^+ emission tends to be strong in areas where the FUV radiation field is strong (see Sect. 3.2).

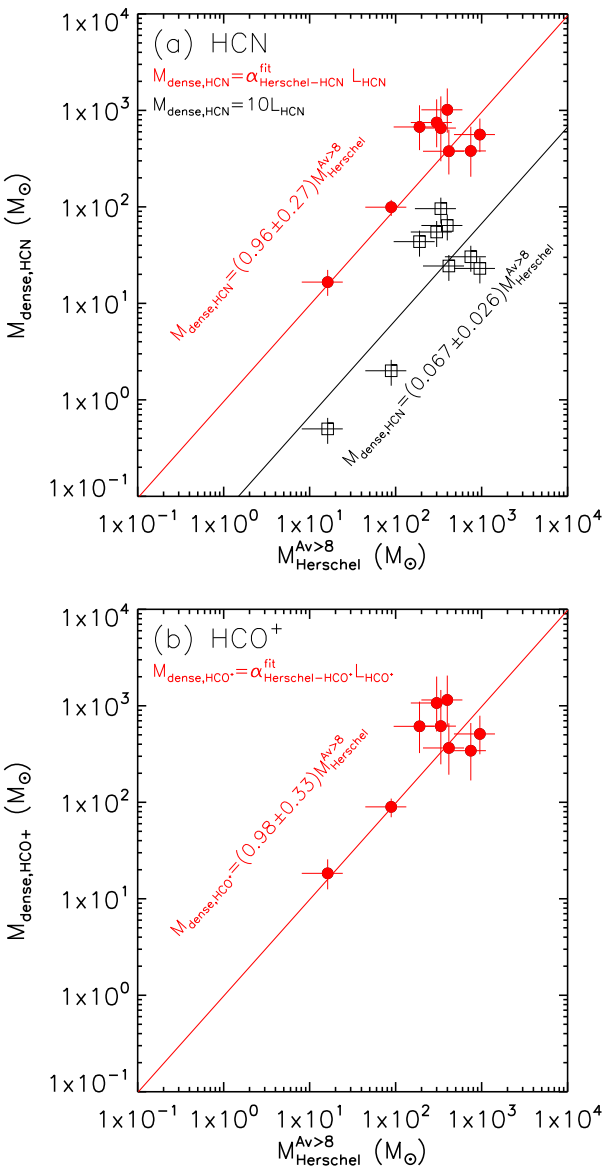

Fig. 5. *a)* $M_{\rm dense,HCN}$ against $M^{A_V>8}_{Herschel}$, and *b)* $M_{\rm dense,HCO^+}$ against $M^{A_V>8}_{Herschel}$. Red lines correspond to best-fit linear relations to the red data points: $M_{\rm dense,HCN} = (0.96 \pm 0.27) \times M^{A_V>8}_{Herschel}$ and $M_{\rm dense,HCO^+} = (0.98 \pm 0.33) \times M^{A_V>8}_{Herschel}$. The red filled circles use $M_{\rm dense,mol}$ values derived from the relation $M_{\rm dense,mol} = \alpha^{\rm fit}_{Herschel-{\rm mol}} \times L_{\rm mol}$. In *panel a*, the black open squares use $M_{\rm dense,HCN}$ values derived from the "extragalactic" relation $M_{\rm dense,HCN} = \alpha_{\rm GS04-HCN} \times L_{\rm HCN}$, where $\alpha_{\rm GS04-HCN} = 10\ M_\odot$ (K km s^{-1} pc^2)$^{-1}$; the black line corresponds to the best-fit linear relation to the open squares: $M_{\rm dense,HCN}$ ($\equiv \alpha_{\rm GS04-HCN}\ L_{\rm HCN}$) $= (0.067 \pm 0.026) \times M^{A_V>8}_{Herschel}$.

The red filled circles in Fig. 4 show a correlation plot between $\alpha_{Herschel-{\rm HCO^+}}$ and G_0. Here again, a clear anti-correlation is present with a correlation coefficient of −0.77. The $\alpha^{\rm fit}_{Herschel-{\rm HCO^+}}$ values are slightly larger than the $\alpha^{\rm fit}_{Herschel-{\rm HCN}}$ values, but the basic trend as a function of G_0 is the same. The $\alpha_{Herschel-{\rm HCO^+}}$ conversion factor decreases as G_0 increases according to the following best-fit relation:

$$\alpha^{\rm fit}_{Herschel-{\rm HCO^+}} = (689 \pm 151) \times G_0^{-0.24 \pm 0.08} \left[M_\odot \left({\rm K\,km\,s^{-1}\,pc^2} \right)^{-1} \right]. \quad (15)$$

Figure 5b plots the mass of dense gas $M_{\rm dense,HCO^+}$ derived from the HCO$^+$ luminosity using the conversion factor $\alpha^{\rm fit}_{Herschel-{\rm HCO^+}}$ from Eq. (15) as a function of the reference mass estimate $M^{A_V>8}_{Herschel}$. As can be seen, the $M_{\rm dense,HCO^+}$ estimates using $\alpha^{\rm fit}_{Herschel-{\rm HCO^+}}$ agree well with the reference dense gas mass estimates $M^{A_V>8}_{Herschel}$.

We conclude that both the HCN(1–0) luminosity and the HCO$^+$(1–0) luminosity can be used as reasonably good tracers of the total mass of dense gas down to molecular cloud scales ≳1 pc, *provided* that appropriate G_0-dependent conversion factors are employed (and the strength of the radiation field can be estimated). This is true despite the fact that the HCN(1–0) and HCO$^+$(1–0) lines are optically thick and do not trace well the details of the filamentary structure of the dense molecular gas (cf. Sect. 3.2).

4.2. Relationship between star-formation rate and dense gas mass

In this subsection, we use our results on nearby clouds, e.g., our finding of a G_0-dependent conversion factor $\alpha_{Herschel}(G_0)$, to make a new detailed comparison between the star-formation efficiency within dense molecular gas found in nearby star-forming complexes on one hand and in external galaxies on the other hand.

4.2.1. Estimates of the star-formation rate and star-formation efficiency in the observed clouds

We first estimated the SFR in each of our target regions/subregions from direct counting of young stellar objects (YSOs) using the available *Spitzer* census of YSOs in nearby clouds (Evans et al. 2009). Under the assumption that the median lifetime of Class II YSOs is 2 Myr (Evans et al. 2009; Covey et al. 2010; Lada et al. 2010; Dunham et al. 2015) and that their mean mass is 0.5 $M_\odot$ (Muench et al. 2007), the SFR can be derived from the number of YSOs observed with *Spitzer* as follows:

$$SFR_{\rm YSO} = 0.25 \times N({\rm YSOs}) \times 10^{-6} \left[M_\odot\,{\rm yr}^{-1} \right]. \quad (16)$$

To evaluate the number of YSOs in each subregion observed here, we used the *Spitzer* catalog of Dunham et al. (2015) for Aquila and Ophiuchus, and the catalog of Megeath et al. (2012) for Orion B. To count YSOs at each evolutionary stage from these catalogs, we selected objects with an infrared spectral index[2] $a_{\rm IR}$ in the ranges $0.3 \leq a_{\rm IR}$ for Class 0/I YSOs, $-0.3 \leq a_{\rm IR} < 0.3$ for Flat Spectrum sources, and $-1.6 \leq a_{\rm IR} < -0.3$ for Class II objects in agreement with standard YSO classification criteria (Greene et al. 1994).

Dunham et al. (2015) used 2MASS and *Spitzer* data between 2 μm and 24 μm. Megeath et al. (2012) used *Spitzer* data between 4.5 μm and 24 μm. While Dunham et al. (2015) published $a_{\rm IR}$ values both before and after correction for extinction, Megeath et al. (2012) used uncorrected $a_{\rm IR}$ values. For the sake of consistency, we used uncorrected $a_{\rm IR}$ values to select Class II YSOs in all regions. The resulting YSO number counts and corresponding SFRs are reported in Table 7 for each region/subregion observed in molecular lines. The blue filled circles in Fig. 7a show the correlation between $\rm SFR_{YSO}$ and $M^{A_V>8}_{Herschel}$ for the clouds of our sample, which can be expressed

[2] The spectral index $a_{\rm IR}$ is defined as the slope of the near-/mid-infrared spectral energy distribution (SED), $a_{\rm IR} = {\rm d}\log(\lambda S_\lambda)/{\rm d}\log(\lambda)$, where λ and S_λ denote wavelength and flux density at that wavelength, respectively.

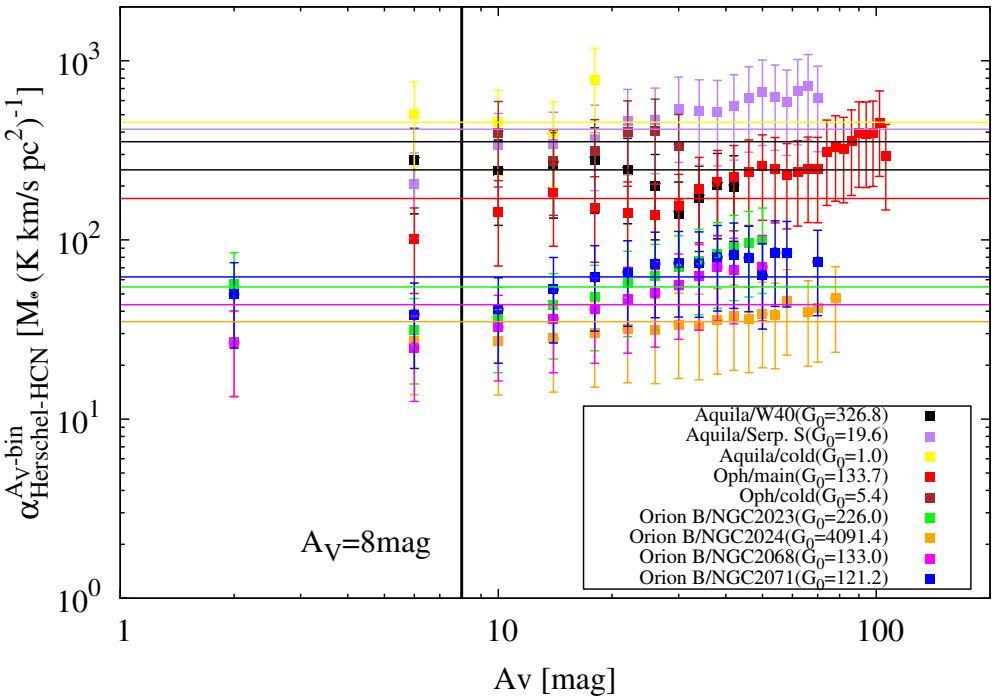

Fig. 6. Empirical conversion factor $\alpha^{\rm A_V-bin}_{Herschel-\rm HCN} \equiv M^{\rm A_V-bin}_{Herschel} \times L^{\rm A_V-bin}_{\rm HCN}$ against column density (expressed in $A_{\rm V}$ units) for the sub-regions of our sample. $M^{\rm A_V-bin}_{Herschel}$ and $L^{\rm A_V-bin}_{\rm HCN}$ represent the mass derived from *Herschel* column density data and the HCN luminosity for the portion of each sub-region corresponding to a given column density bin. The width of each column density bin is 4 mag in $A_{\rm V}$ units. The horizontal lines indicate $\alpha_{Herschel-\rm HCN}$ for the various regions (see Table 6).

Table 7. Number of YSOs and star-formation rate in each subregion.

Region	N(YSOs)†	$SFR_{\rm YSO}$ [$M_\odot$ yr^{-1}]‡
Aquila/W40	88–115	(22.0–28.8) $\times 10^{-6}$
Aquila/Serp S	57–139	(14.2–34.8) $\times 10^{-6}$
Aquila/cold	11–15	(2.8–3.8) $\times 10^{-6}$
Aquila (total)	156–269	(39.0–67.3) $\times 10^{-6}$
Oph/main (L1688)	60–112	(15.0–28.0) $\times 10^{-6}$
Oph/cold	0–0	–
Oph (total)	60–112	(15.0–28.0) $\times 10^{-6}$
Orion B/NGC2023	9–15	(2.2–3.8) $\times 10^{-6}$
Orion B/NGC2024	37–55	(9.2–13.8) $\times 10^{-6}$
Orion B/NGC2068	6–12	(1.5–3.0) $\times 10^{-6}$
Orion B/NGC2071	26–43	(6.5–10.8) $\times 10^{-6}$
Orion B (total)	78–125	(19.5–31.3) $\times 10^{-6}$

Notes. $^{(\dagger)}$ Number of YSOs in each subregion observed in HCN, HCO$^+$, H^{13}CN, and H^{13}CO$^+$. The lower value gives the number of Class II YSOs, the upper value the combined number of Class 0/I, Flat, and Class II YSOs. $^{(\ddagger)}$ The uncertainties are $\sqrt{N}$ statistical uncertainties, where N is the number count.

as $SFR_{\rm YSO} = (2.1–5.0)\times 10^{-8}\ M_\odot\ {\rm yr}^{-1} \times (M^{\rm A_V>8}_{Herschel}/M_\odot)$. This relationship is in good agreement with previous studies of nearby Galactic clouds using extinction maps to estimate the mass of dense gas (Lada et al. 2010, 2012; Evans et al. 2014).

4.2.2. Calibration of the dense gas mass in external galaxies

In Sect. 4.1, we showed that reliable HCN-based estimates of the dense gas mass in nearby clouds could be obtained using the G_0-dependent conversion factor $\alpha^{\rm fit}_{Herschel-\rm HCN}(G_0)$ given by Eq. (14). In this subsection, we try to account for this G_0 dependence in galaxies with published HCN data in an effort to improve the current estimates of their dense gas masses. Before doing so, it is important to notice that the $\alpha^{\rm fit}_{Herschel-\rm HCN}(G_0)$ values derived for the nearby clouds of our sample are a factor of $\gtrsim$3 to ~50 higher than the standard extragalactic conversion factor $\alpha_{\rm GS04-HCN} = 10\ M_\odot\ ({\rm K\,km\,s^{-1}\,pc^2})^{-1}$ (see Fig. 4). Since the mean G_0 value in a typical galaxy cannot be much higher than the highest G_0 found in our regions ($G_0 \sim 4000$ for NGC 2024), another effect besides the G_0 dependence must explain this large difference in conversion factor.

While our HCN/HCO$^+$ observations were specifically focused on the densest ($A_{\rm V} > 8$) portions of the target clouds, they also cover a small fraction of the lower density gas in these clouds, and our data clearly show that the HCN(1–0) and HCO$^+$(1–0) lines are tracing molecular gas down to much lower column densities than the $A_{\rm V} = 8$ fiducial limit. In a recent independent molecular line study of the southern part of the Orion B cloud (including NGC 2023 and NGC 2024) with the IRAM 30 m telescope, Pety et al. (2017) found that 36% of the HCN(1–0) line flux was emitted from low extinction ($2 \leq A_{\rm V} < 6$) areas, with >98% of the line flux coming from $A_{\rm V} \geq 2$ areas. Likewise, the results of the CHaMP census of molecular clumps in the southern Milky Way with the MOPRA telescope (e.g., Barnes et al. 2016) demonstrate that the HCO$^+$(1–0) line emission is generally tracing gas down to volume densities of ~10^3 cm^{-3} or less. Dividing the regions and sub-regions observed in our study in various column density bins, we can investigate possible variations of the empirical conversion factor $\alpha^{\rm A_V-bin}_{Herschel-\rm HCN} \equiv M^{\rm A_V-bin}_{Herschel} \times L^{\rm A_V-bin}_{\rm HCN}$ with column density (see Fig. 6). Significant variations in $\alpha^{\rm A_V-bin}_{Herschel-\rm HCN}$ from region to region can be seen, in agreement with the dependence of $\alpha_{Herschel-\rm HCN}$ on the strength of the FUV radiation

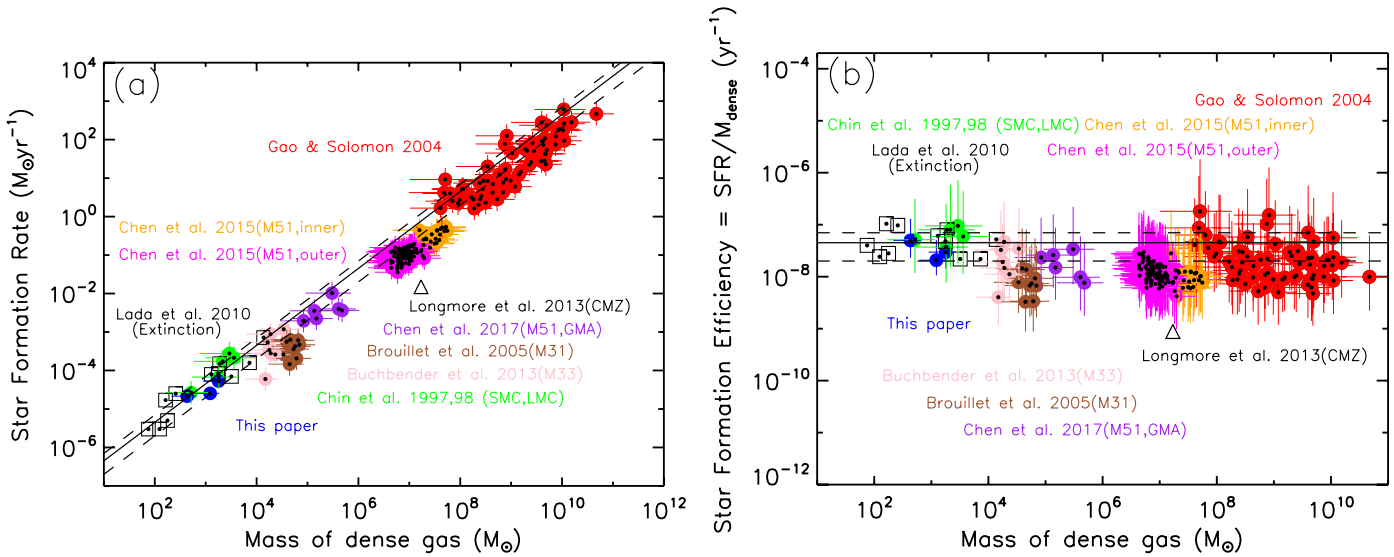

Fig. 7. *a)* SFR against $M_{\rm dense}$ and *b)* SFE against $M_{\rm dense}$. Blue filled squares indicate the SFR–$M_{\rm dense}(=M_{Herschel}^{A_{\rm V}>8})$ and SFE$(=SFR/M_{\rm dense})$ – $M_{\rm dense}$ relations for the regions observed in this paper. Black open circles indicate the relation between SFR and $M_{\rm dense}$ in nearby star-forming clouds (Lada et al. 2010). Red filled circles indicate the SFR-$M_{\rm dense}$ and SFE – $M_{\rm dense}$ relations obtained for external galaxies (Gao & Solomon 2004b), assuming $M_{\rm dense} = \alpha_{\rm HCN} \times L_{\rm HCN}$ with the corrected $\alpha_{\rm HCN}$ values from our Eq. (17). Green, brown, pink, purple, magenta, and orange filled circles indicate the SFR-$M_{\rm dense}$ and SFE – $M_{\rm dense}$ relations in the SMC, LMC, M31, M33, and M51 galaxies (Chin et al. 1997, 1998; Brouillet et al. 2005; Buchbender et al. 2013; Chen et al. 2015, 2017) using our relation of Eq. (17). The uncertainties in the extragalactic SFR values are a factor of ~2 (cf. Bell 2003). The black triangle indicates the position of the central molecular zone (CMZ: $|l| < 1$ deg, $|b| < 0.5$ deg) in each plot, where SFR and $M_{\rm dense}$ were estimated from the number count of massive YSOs and *Herschel* column density, respectively (Longmore et al. 2013). In both panels, the black solid line and black dashed lines display the simple empirical relation expected from the "microphysics" of prestellar core formation within filaments described in Sect. 4.3 (see also André et al. 2014; Könyves et al. 2015): $SFR = (4.5 \pm 2.5) \times 10^{-8}\ M_\odot\,{\rm yr}^{-1} \times (M_{\rm dense}/M_\odot)$, i.e., $SFE = (4.5 \pm 2.5) \times 10^{-8}\ {\rm yr}^{-1}$.

field discussed in Sect. 4.1. Figure 6 nevertheless suggests that, in any given sub-region (i.e., for a given G_0 value), the conversion between gas mass and HCN(1–0) luminosity remains approximately constant, irrespective of gas (column) density or $A_{\rm V}$, down to $A_{\rm V} \sim 2$. This means that, in addition to the dense molecular gas $n_{\rm H_2} \gtrsim 2 \times 10^4$ cm^{-3} (corresponding to $A_{\rm V} \gtrsim 8$ in resolved nearby clouds), extragalactic HCN(1–0) studies with spatial resolutions from ~8 pc to ~36 kpc (Chin et al. 1997, 1998; Gao & Solomon 2004b; Brouillet et al. 2005; Buchbender et al. 2013; Chen et al. 2015, 2017) must also probe essentially all of the molecular gas corresponding to $2 < A_{\rm V} < 8$ in the observed galaxies. Using typical column density probability distribution functions (PDFs) observed toward Galactic molecular clouds (e.g., Schneider et al. 2013), we can estimate the relative amount of molecular gas at $A_{\rm V} > 8$ and $2 < A_{\rm V} \leq 8$ in GMCs, $M(A_{\rm V} > 2)/M(A_{\rm V} > 8)$. In practice, we adopt the combined column density PDF derived from *Herschel* HGBS data in the Aquila and Orion B complexes, which is well described by a power law, ${\rm d}N/{\rm dlog}N_{\rm H_2} \propto N_{\rm H_2}^{-2.7\pm0.2}$ (Könyves et al. 2015, and in prep.), as our template. Such a column density PDF implies that $M(A_{\rm V} > 2)/M(A_{\rm V} > 8) = (2/8)^{-1.7\pm0.2} \approx 10$, at least in molecular clouds such as Aquila and Orion B. Clearly, if extragalactic HCN measurements of dense gas include low-density gas down to $A_{\rm V} \sim 2$, then the effective $\alpha_{\rm HCN}$ conversion factor for these measurements must be an order of magnitude lower than the $\alpha^{\rm fit}_{Herschel-{\rm HCN}}(G_0)$ factor given by Eq. (14) and thus within a factor of a few of the standard extragalactic conversion factor $\alpha_{\rm GS04-HCN} = 10\ M_\odot\ ({\rm K\,km\,s^{-1}\,pc^2})^{-1}$.

To go further and to improve current extragalactic $M_{\rm dense,HCN}$ estimates for radiation-field effects, we also need to account for the fact that the minimum column density or extinction $A_{V,\rm min}$(HCN) down to which significant HCN(1–0) line flux is emitted itself depends on G_0. The values of the effective excitation density of HCN(1–0) calculated by Shirley (2015) scale approximately as $n_{\rm eff}^{\rm HCN} \propto T_{\rm gas}^{-0.65}$, where $T_{\rm gas}$ is the gas kinetic temperature. Assuming $T_{\rm gas} \approx T_{\rm dust}$ and using the simplified relation between $T_{\rm dust}$ and G_0 given by Eq. (12), this means that $n_{\rm eff}^{\rm HCN} \propto G_0^{-0.13}$. For both a spherical and a cylindrical cloud with a density gradient $\rho \propto r^{-\alpha}$, column density scales as $r^{1-\alpha}$ or $\rho^{1-\frac{1}{\alpha}}$. Adopting $\alpha = 1.75 \pm 0.25$, a value intermediate between 1.5 (free-falling cloud onto a point mass) and 2 (isothermal spheres) which is also consistent with the logarithmic slope of −2.7 for the column density PDF (cf. Könyves et al. 2015), we may thus expect the minimum column density probed by HCN(1–0) to scale as $A_{V,\rm min}({\rm HCN}) \propto (n_{\rm eff}^{\rm HCN})^{0.43} \propto G_0^{-0.056\pm0.012}$. Normalizing this scaling relation using the fact that $A_{V,\rm min}({\rm HCN}) \approx 2$ for NGC 2023/2024 in Orion B where $G_0 \approx 20$ (Pety et al. 2017), we obtain the following $\alpha^{\rm fit'}_{Herschel-{\rm HCN}}$ conversion factor for external galaxies, under the assumption that extragalactic HCN observations sample all of the molecular gas down to $A_{V,\rm min}$(HCN):

$$\alpha^{\rm fit'}_{Herschel-{\rm HCN}} \approx 0.13^{+0.06}_{-0.06} \times G_0^{-0.095\pm0.02} \times \alpha^{\rm fit}_{Herschel-{\rm HCN}} \propto G_0^{-0.34\pm0.08}. \quad (17)$$

Using the total infrared luminosities $L_{\rm IR}$ listed in the Gao & Solomon (2004b) paper and adopting $L_{\rm FIR} = L_{\rm IR}/1.3$ (Graciá-Carpio et al. 2008), we can derive relevant G_0 values from Eq. (9) and $I_{\rm FIR} = L_{\rm FIR}/4\pi d^2(\frac{\pi\theta^2_{\rm beam}}{4\ln 2})$, where d and $\theta_{\rm beam}$ are the distance to each galaxy and the telescope beam size of the corresponding HCN measurement respectively (cf. Buchbender et al. 2013). We can then estimate an effective conversion factor $\alpha^{\rm fit'}_{Herschel-{\rm HCN}}(G_0)$ for each galaxy in the Gao & Solomon sample. The resulting G_0 and $\alpha^{\rm fit'}_{Herschel-{\rm HCN}}$ values range from 44

to 3.9×10^4 (mean: 1.7×10^3) and from 1.8 $M_\odot$ (K km s^{-1} pc^2)$^{-1}$ to 17.7 $M_\odot$ (K km s^{-1} pc^2)$^{-1}$ (mean: 10.2 $M_\odot$ (K km s^{-1} pc^2)$^{-1}$), respectively. Using these $\alpha^{\rm fit'}_{Herschel-{\rm HCN}}$ values for the HCN conversion factor, the corrected masses of dense gas range from 4.3×10^7 $M_\odot$ to 4.9×10^{10} $M_\odot$. Under the assumption that the average gas densities of normal galaxies and extreme starbursts are 2×10^2 cm^{-3} and 1×10^5 cm^{-3}, respectively, García-Burillo et al. (2012) advocated revised conversion factors $\alpha_{\rm GB12-HCN}\sim3$–4 $M_\odot$ (K km s^{-1} pc^2)$^{-1}$ for normal galaxies ($L_{\rm IR}<10^{11}$ $L_\odot$ corresponding to $SFR<2\times10$ $M_\odot$ yr^{-1}) and $\alpha_{\rm GB12-HCN}\sim1$–2 $M_\odot$ (K km s^{-1} pc^2)$^{-1}$ for extreme starbursts ($L_{\rm IR}>10^{11}$ $L_\odot$ corresponding to $SFR>2\times10$ $M_\odot$ yr^{-1}). The revised conversion factors $\alpha_{\rm GB12-HCN}$ of García-Burillo et al. (2012) are roughly consistent with our suggested $\alpha^{\rm fit'}_{Herschel-{\rm HCN}}$ values of 1.8–17.7 $M_\odot$ (K km s^{-1} pc^2)$^{-1}$ for the galaxies sampled by Gao & Solomon (2004b) ($L_{\rm IR}\sim10^{10-12}$ $L_\odot$). This agreement suggests that the dependence of the $\alpha_{Herschel-{\rm HCN}}$ conversion factor on the strength of the FUV radiation field is not restricted to Galactic clouds and also applies to external galaxies. Figure 7a compiles observations of the SFR–$M_{\rm dense}$ relation from the present study, Lada et al. (2010), and Gao & Solomon (2004b). The SFR-$M_{\rm dense}$ relation found in our study is consistent with that of Lada et al. (2010), as expected since both are focused on nearby Galactic clouds. The initial SFR-$M_{\rm dense}$ relation from Gao & Solomon (2004b) lies a factor of ~2–3 below the best-fit relation found for nearby star-forming regions, namely $SFR=4.6\times10^{-8}$ $M_{\rm dense}$ (Lada et al. 2010). Conversely, the corrected SFR-$M_{\rm dense}$ relation for the Gao & Solomon (2004b) sample lies above the nearby-cloud relation by a factor of ~3. We also compiled data points for nearby galaxies of the local group, namely the Small Magellanic Cloud (SMC), the Large Magellanic Cloud (LMC), M31, M33, and M51 from Chin et al. (1997, 1998), Brouillet et al. (2005), Buchbender et al. (2013), and Chen et al. (2015, 2017). The SFR for each galaxy was estimated using $SFR=2.0\times10^{-10}$ ($L_{\rm IR}/L_\odot$) $M_\odot$ yr^{-1} following Gao & Solomon (2004b). As can be seen in Fig. 7a, the observed trend is basically a linear relation between SFR and dense gas mass, and the nearby-cloud relation provides a good overall fit to most data points.

Figure 7b provides a blow-up view of the scatter around the nearby-cloud star formation law by plotting the star-formation efficiency $SFE_{\rm dense}\equiv SFR/M_{\rm dense}$ against $M_{\rm dense}$ for the same objects as in Fig. 7a. As can be seen, SFE$_{\rm dense}$ remains roughly constant within a scatter of less than 1.5 orders of magnitude over 8 orders of magnitude in $M_{\rm dense}$ from ~10^2 $M_\odot$ to 10^{10} $M_\odot$. This scatter in SFE$_{\rm dense}$ is significantly smaller than the scatter in SFE$_{\rm total}$, defined as SFR divided by total molecular gas mass $M_{\rm total}$, observed among nearby clouds and massive Galactic clouds, which exceeds 2 to 3 orders of magnitude over only 4 orders of magnitude in gas mass (cf. Lada et al. 2010; Vutisalchavakul et al. 2016). The mean and standard deviation of (the logs of) all the data points in Fig. 7b (including the CMZ point) are $\langle\log SFE_{\rm dense}$ (yr^{-1})$\rangle=-7.85\pm0.31$. This is in excellent agreement with the results of Vutisalchavakul et al. (2016) who found $\langle\log SFE_{\rm dense}$ (yr^{-1})$\rangle=-7.74\pm0.50$ toward star-forming regions in the Galactic plane using masses derived from the Bolocam Galactic Plane Survey (BGPS) data at 1.1 mm and SFR values estimated from WISE mid-infrared data.

The vertical scatter in Fig. 7b can almost entirely be attributed to uncertainties in the $\alpha_{\rm HCN}$ conversion factor used to estimate the dense gas mass for galaxies. In nearby clouds, for which assumptions about this conversion factor are not needed, the observed scatter in SFE$_{\rm dense}$ is less than a factor of ~3. To conclude, our results support the view that the relationship between star-formation rate and dense gas mass, i.e., the star-formation efficiency in the dense molecular gas of galaxies, is quasi-universal on a wide range of scales from ~1–10 pc to >10 kpc.

4.3. Origin of the quasi-universal star-formation efficiency in dense molecular gas

On the grounds that filaments dominate the mass budget of dense molecular gas in GMCs and that most, if not all, prestellar cores form in filaments (see Sect. 1), André et al. (2014) proposed that the quasi-universal star-formation efficiency in dense gas discussed above and summarized in Fig. 7 originates from the physics of filament evolution and core formation along filaments. Following André et al. (2014), we suggest that the star-formation efficiency in dense gas, $SFE_{\rm dense}\equiv{\rm SFR}/M_{\rm dense}$, is primarily set by three parameters characterizing dense cores along filaments, namely the typical fraction of dense filament gas in the form of prestellar cores (or "core formation efficiency"), $f_{\rm pre}$, the typical lifetime of prestellar cores, $t_{\rm pre}$, and the efficiency of the conversion from prestellar core mass to stellar mass (or stellar system mass), $\epsilon_{\rm core}$, according to the simple relation: $SFE_{\rm dense}=f_{\rm pre}\times\epsilon_{\rm core}/t_{\rm pre}$. This relation assumes that, in steady state, each supercritical filament has converted a fraction $f_{\rm pre}$ of its mass into prestellar cores, and that each prestellar core converts a fraction $\epsilon_{\rm core}$ of its mass into either a single star or a small stellar system on a timescale $t_{\rm pre}$. The latter assumption is supported by the similarity between the prestellar core mass function (CMF) and the stellar initial mass function (IMF; e.g., Motte et al. 1998; Enoch et al. 2008; André et al. 2010). Observationally, it seems that the three parameters $f_{\rm pre}$, $t_{\rm pre}$, $\epsilon_{\rm core}$ have reasonably constant values with little variations from cloud to cloud, at least in Gould Belt regions. Based on the results of the HGBS in the Aquila, Ophiuchus, Orion B, and Taurus/L1495 clouds, the prestellar core formation efficiency in the dense ($A_{\rm V}>8$) gas of supercritical filaments is estimated to be $f_{\rm pre}=15\%^{+5\%}_{-5\%}$ (e.g., Könyves et al. 2015; Könyves et al., in prep.; Ladjelate et al., in prep.). The typical lifetime of low- to intermediate-mass prestellar cores is known to be $t_{\rm pre}=1^{+0.5}_{-0.3}$ Myr (e.g., Lee & Myers 1999; Jessop & Ward-Thompson 2000; Könyves et al. 2015). In reality, $t_{\rm pre}$ likely depends on both core density (Jessop & Ward-Thompson 2000) and core mass (Hatchell & Fuller 2008), but what matters here is the characteristic lifetime of the bulk of prestellar cores near the peak of the CMF and forming in filaments just above the critical line mass $M_{\rm line,crit}$. The efficiency of the conversion process from core mass to stellar mass, as estimated from the global shift between the CMF and the IMF is believed to be $\epsilon_{\rm core}=30\%^{+20\%}_{-10\%}$ (e.g., Alves et al. 2007; Nutter & Ward-Thompson 2007; Könyves et al. 2015). Combining these estimates leads to the following "prediction" for SFE$_{\rm dense}$ from the microphysics of star formation in filaments:

$$SFE^{\rm pre}_{\rm dense}\equiv f_{\rm pre}\times\epsilon_{\rm core}/t_{\rm pre}=(4.5\pm2.5)\times10^{-8}\ {\rm yr}^{-1}, \quad (18)$$

which is plotted as a solid straight line and strip in Fig. 7. As can be seen, SFE$^{\rm pre}_{\rm dense}$ provides a reasonably good fit to both the Galactic and extragalactic data points of Fig. 7b.

4.4. Comments on apparent SFE variations in resolved galactic disks

Recently, Usero et al. (2015), Chen et al. (2015), and Bigiel et al. (2016) reported significant variations in the apparent

star-formation efficiency in dense gas, $SFE_{\rm dense}^{\rm extragal} \equiv L_{\rm FIR}/L_{\rm HCN}$, across the spatially-resolved disks of several nearby galaxies such as M51. In particular, the $L_{\rm FIR}/L_{\rm HCN}$ ratio was observed to decrease as $L_{\rm FIR}$ increases from the outskirts to the center of the M51 disk (see for instance the map of the $L_{\rm IR}/L_{\rm HCN}$ ratio presented by Chen et al. 2015). One plausible interpretation of this trend was a decrease in the star-formation efficiency $\rm SFE_{dense}$ from the outer disk to the center of the M51 galaxy (e.g., Bigiel et al. 2016). We note, however, that since the FUV radiation field is significantly stronger near the center of the disk compared to the outer parts of the galaxy, and since $L_{\rm IR}/L_{\rm HCN}$ scales as $\frac{SFR}{M_{\rm dense}} \times \alpha_{\rm HCN} = SFE_{dense} \times \alpha_{\rm HCN}$, the trend observed in M51 can at least partly originate from the expected decrease in the $\alpha_{\rm HCN}$ factor toward the center of the disk according to Eq. (14), with the efficiency $\rm SFE_{dense}$ remaining approximately constant.

We can further quantify this statement using the detailed results published by Usero et al. (2015) for 29 nearby disk galaxies. These authors found an anti-correlation between the apparent local star-formation efficiency in dense gas $SFE_{\rm Usero-dense} \equiv I_{\rm FIR}/I_{\rm HCN}$ and the mass surface density of stars $\Sigma_{\rm star}$, expressed as $SFE_{\rm Usero-dense}$ (Myr^{-1}) $= 10^{-0.78\pm0.30}\ \Sigma_{\rm Usero-star}^{-0.37\pm0.11}$ ($M_\odot$ pc^{-2}) (Fig. 2 of Usero et al. 2015). Usero et al. (2015) evaluated the mass surface density of dense gas $\Sigma_{\rm dense}$ as $\alpha_{\rm Usero-HCN} \times I_{\rm HCN}$ and the mass surface density of old stars $\Sigma_{\rm Usero-star}$ values from the 3.6 μm intensity $I_{3.6\,\mu\rm m}$ (with $\Sigma_{\rm Usero-star} \propto I_{3.6\,\mu\rm m}$). Since the $I_{3.6\,\mu\rm m}$ intensity is directly proportional to the FUV intensity $I_{\rm FUV}$ across the disk of nearby galaxies (e.g., Ford et al. 2013), the anti-correlation $SFE_{\rm Usero-dense} \propto \Sigma_{\rm Usero-star}^{-0.37\pm0.11}$ can be rewritten as $SFE_{\rm dense} \times \alpha_{\rm Usero-HCN} \propto I_{\rm FUV}^{-0.37\pm0.11}$. The dependence of $\alpha_{\rm HCN}$ on G_0 found in Sects. 4.1 and 4.2.2 and expressed by Eq. (17), i.e., $\alpha_{Herschel-\rm HCN}^{\rm fit'} \propto G_0^{-0.34\pm0.08}$, can largely account for the Usero et al. (2015) anti-correlation, and suggests that $\rm SFE_{dense}$ actually depends at most very weakly on $\Sigma_\star$ as $SFE_{\rm dense} \propto \Sigma_\star^{-0.03\pm0.13}$.

Significant variations in $\rm SFE_{dense}$ may still exist in the most extreme star-forming environments like the central molecular zone (CMZ) of our Milky Way (e.g., Longmore et al. 2013, see also Fig. 7) or extreme starburst galaxies (e.g., García-Burillo et al. 2012), especially at high redshift (e.g., Gao et al. 2007). By and large, however, the results summarized in Fig. 7b suggest that $\rm SFE_{dense}$ is remarkably constant over a wide range of scales and environments.

5. Summary and conclusions

In an effort to calibrate dense gas tracers commonly used in extragalactic studies, we carried out wide-field mapping observations at a spatial resolution of ~0.04 pc in HCN (J = 1–0), $\rm H^{13}CN$ (J = 1–0), $\rm HCO^+$ (J = 1–0), and $\rm H^{13}CO^+$ (J = 1–0) toward the nearby molecular clouds in Ophiuchus, Aquila, and Orion B using the MOPRA 22 m, IRAM 30 m, and Nobeyama 45 m telescopes. Our main results can be summarized as follows:

1. The spatial distributions of the $\rm H^{13}CO^+$(1–0) and $\rm H^{13}CN$(1–0) emission are tightly correlated with the filamentary texture of the dense gas seen in *Herschel* column density maps, showing that the $\rm H^{13}CO^+$(1–0) and $\rm H^{13}CN$(1–0) lines are good tracers of the densest ("supercritical") filaments seen in *Herschel* submillimeter continuum images. Quantitatively, $\rm H^{13}CO^+$(1–0) and $\rm H^{13}CN$(1–0) trace *Herschel* filaments very well above $A_{\rm V} > 16$ (i.e., $M_{\rm line} \gtrsim 30\ M_\odot\,{\rm pc}^{-1}$) and $A_{\rm V} > 20$ (i.e., $M_{\rm line} \gtrsim 40\ M_\odot\,{\rm pc}^{-1}$) respectively. Moreover, the virial mass estimates derived from the $\rm H^{13}CO^+$(1–0) and $\rm H^{13}CN$(1–0) velocity dispersions agree well with the dense gas mass estimates derived from *Herschel* data for the same sub-regions.
2. In contrast, the spatial distributions of the HCN(1–0) and $\rm HCO^+$(1–0) emission differ significantly from the column density distribution derived from *Herschel* data. The HCN(1–0) and $\rm HCO^+$ (1–0) lines are only poor tracers of the supercritical filaments seen with *Herschel* and tend to be stronger around HII regions. Based on a detailed comparison of the HCN(1–0)and $\rm HCO^+$(1–0) integrated intensity maps with the *Herschel* 70/100 μm and dust temperature maps, it appears that the HCN(1–0) and $\rm HCO^+$(1–0) integrated intensities are strongly correlated with the strength of the local FUV radiation field (G_0). The luminosities of the HCN and $\rm HCO^+$ lines can nevertheless be used to derive reasonably good estimates of the masses of dense gas in the nearby clouds we observed, *provided* that appropriate G_0-dependent conversion factors $\alpha_{Herschel-\rm HCN}(G_0)$ and $\alpha_{Herschel-\rm HCO^+}(G_0)$ are adopted when converting $L_{\rm HCN}$ and $L_{\rm HCO^+}$ to $M_{\rm dense}$.
3. Using the masses $M_{Herschel}^{A_{\rm V}>8}$ derived from *Herschel* column density maps above $A_{\rm V} > 8$ as reference estimates of the mass of dense gas in each nearby cloud, we found that the conversion factors $\alpha_{\rm HCN}$ and $\alpha_{\rm HCO^+}$ are anti-correlated with the strength of the local FUV radiation field according to the following best-fit empirical relations: $\alpha_{Herschel-\rm HCN}^{\rm fit} = (496 \pm 94) \times G_0^{-0.24\pm0.07}\ M_\odot\ ({\rm K\,km\,s^{-1}\,pc^2})^{-1}$ and $\alpha_{Herschel-\rm HCO^+}^{\rm fit} = (689 \pm 151) \times G_0^{-0.24\pm0.08}\ M_\odot\ ({\rm K\,km\,s^{-1}\,pc^2})^{-1}$.
4. The relation between the star-formation rate, estimated from direct counting of *Spitzer* YSOs, and the mass of dense gas, derived from *Herschel* data above $A_{\rm V} > 8$, for the nearby clouds/clumps of our sample can be expressed as $SFR_{\rm YSO} = (2.1\text{–}5.0)\times10^{-8}\ M_\odot\,{\rm yr}^{-1} \times (M_{Herschel}^{A_{\rm V}>8}/M_\odot)$. This is consistent within errors with the relation found by Lada and collaborators for another and broader sample of nearby star-forming clouds based on *Spitzer* and near-infrared extinction data ($SFR = (4.6 \pm 2.6) \times 10^{-8}\ M_\odot\,{\rm yr}^{-1} \times (M_{\rm dense}/M_\odot)$, Lada et al. 2010, 2012).
5. In nearby molecular clouds, the optically thick HCN(1–0) and $\rm HCO^+$(1–0) lines are tracing both moderate column density areas ($2 \leq A_{\rm V} \leq 8$) and high column density areas ($A_{\rm V} > 8$) (see also Pety et al. 2017). Therefore, published extragalactic HCN(1–0) studies, which have spatial resolutions between ~10 pc and ~50 kpc, must be tracing all of the moderate density gas down to $n_{\rm H_2} \lesssim 10^3$ cm^{-3} in the observed galaxies, in addition to the dense gas with $n_{\rm H_2} > 10^4$ cm^{-3}. Estimating the contribution of this moderate density gas from the typical column density PDFs observed in nearby clouds, we obtained the following effective HCN conversion factor for external galaxies: $\alpha_{Herschel-\rm HCN}^{\rm fit'} = 0.13^{+0.06}_{-0.06} \times G_0^{-0.095\pm0.02} \times \alpha_{Herschel-\rm HCN}^{\rm fit}(G_0) \propto G_0^{-0.34\pm0.08}$.
6. Using this G_0-dependent conversion factor $\alpha_{Herschel-\rm HCN}^{\rm fit'}(G_0)$ to improve the dense gas mass estimates of external galaxies with published HCN data, we found that the star-formation efficiency in dense molecular gas, $SFE_{\rm dense} \equiv SFR/M_{\rm dense}$, is remarkably constant, with a scatter of less than 1.5 orders of magnitude around the nearby-cloud value of 4.5×10^{-8} yr^{-1}, over 8 orders of magnitude in $M_{\rm dense}$ from ~$10^2\ M_\odot$ to $10^{10}\ M_\odot$. This suggests that the star-formation efficiency in the dense molecular gas of galaxies is quasi-universal on a wide range of scales from ~1–10 pc to >10 kpc.
7. Following André et al. (2014), we suggest that $\rm SFE_{dense}$ is primarily set by three parameters characterizing the "microphysics" of core/star formation along molecular filaments,

namely the typical fraction of dense filament gas in the form of prestellar cores, $f_{\rm pre} = 15\%^{+10\%}_{-5\%}$, the typical lifetime of solar-type prestellar cores, $t_{\rm pre} = 1^{+0.5}_{-0.3}$ Myr, and the efficiency of the conversion from prestellar core mass to stellar mass, $\epsilon_{\rm core} = 30\%^{+20\%}_{-10\%}$, according to the simple relation: $SFE^{\rm pre}_{\rm dense} = f_{\rm pre} \times \epsilon_{\rm core}/t_{\rm pre} = (4.5 \pm 2.5) \times 10^{-8}$ yr^{-1}.

Acknowledgements. We thank the referee for useful suggestions that improved the clarity of the paper. The Mopra radio telescope is part of the Australia Telescope National Facility which is funded by the Australian Government for operation as a National Facility managed by CSIRO. The 45-m radio telescope is operated by Nobeyama Radio Observatory, a branch of National Astronomical Observatory of Japan. This research has made use of data from the Herschel Gould Belt survey (HGBS) project (`http://gouldbelt-herschel.cea.fr`). The HGBS is a Herschel Key Programme jointly carried out by SPIRE Specialist Astronomy Group 3 (SAG 3), scientists of several institutes in the PACS Consortium (CEA Saclay, INAF-IFSI Rome and INAF-Arcetri, KU Leuven, MPIA Heidelberg), and scientists of the Herschel Science Center (HSC). Our work was supported by the ANR-11-BS56-010 project "STARFICH" and the European Research Council under the European Union's Seventh Framework Programme (ERC Advanced Grant Agreement No. 291294 – "ORISTARS"). N.S. acknowledges support from the DFG through project number Os 177/2-1 and 177/2-2, and central funds of the DFG-priority program 1573 (ISM-SPP). Y.G. acknowledges support from the National Natural Science Foundation of China (grants 11390373 and 11420101002) and the Chinese Academy of Sciences' Key Research Program of Frontier Sciences.

References

Alves, J., Lombardi, M., & Lada, C. J. 2007, A&A, 462, L17
André, P., Montmerle, T., Feigelson, E. D., Stine, P. C., & Klein, K.-L. 1988, ApJ, 335, 940
André, P., Ward-Thompson, D., & Barsony, M. 2000, in Protostars and Planets IV (Tucson: University of Arizona Press), 59
André, P., Men'shchikov, A., Bontemps, S., et al. 2010, A&A, 518, L102
André, P., Di Francesco, J., Ward-Thompson, D., et al. 2014, in Protostars and Planets VI (Tucson: University of Arizona Press), 27
Arzoumanian, D., André, P., Didelon, P., et al. 2011, A&A, 529, L6
Barnes, P. J., Hernandez, A. K., O'Dougherty, S. N., Schap, III, W. J., & Muller, E. 2016, ApJ, 831, 67
Bell, E. F. 2003, ApJ, 586, 794
Bigiel, F., Leroy, A. K., Jiménez-Donaire, M. J., et al. 2016, ApJ, 822, L26
Bohlin, R. C., Savage, B. D., & Drake, J. F. 1978, ApJ, 224, 132
Braine, J., Shimajiri, Y., André, P., et al. 2017, A&A, 597, A44
Brouillet, N., Muller, S., Herpin, F., Braine, J., & Jacq, T. 2005, A&A, 429, 153
Buchbender, C., Kramer, C., Gonzalez-Garcia, M., et al. 2013, A&A, 549, A17
Chen, H., Gao, Y., Braine, J., & Gu, Q. 2015, ApJ, 810, 140
Chen, H., Braine, J., Gao, Y., Koda, J., & Gu, Q. 2017, ApJ, 836, 101
Chin, Y.-N., Henkel, C., Whiteoak, J. B., et al. 1997, A&A, 317, 548
Chin, Y.-N., Henkel, C., Millar, T. J., Whiteoak, J. B., & Marx-Zimmer, M. 1998, A&A, 330, 901
Covey, K. R., Lada, C. J., Román-Zúñiga, C., et al. 2010, ApJ, 722, 971
Drew, J. E., Busfield, G., Hoare, M. G., et al. 1997, MNRAS, 286, 538
Dunham, M. M., Allen, L. E., Evans, II, N. J., et al. 2015, ApJS, 220, 11
Dzib, S., Loinard, L., Mioduszewski, A. J., et al. 2010, ApJ, 718, 610
Emerson, D. T., & Graeve, R. 1988, A&A, 190, 353
Enoch, M. L., Evans, II, N. J., Sargent, A. I., et al. 2008, ApJ, 684, 1240
Evans, II, N. J., Dunham, M. M., Jørgensen, J. K., et al. 2009, ApJS, 181, 321
Evans, II, N. J., Heiderman, A., & Vutisalchavakul, N. 2014, ApJ, 782, 114
Ford, G. P., Gear, W. K., Smith, M. W. L., et al. 2013, ApJ, 769, 55
Gao, Y., & Solomon, P. M. 2004a, ApJS, 152, 63
Gao, Y., & Solomon, P. M. 2004b, ApJ, 606, 271
Gao, Y., Carilli, C. L., Solomon, P. M., & Vanden Bout, P. A. 2007, ApJ, 660, L93
García-Burillo, S., Usero, A., Alonso-Herrero, A., et al. 2012, A&A, 539, A8
Gibb, A. G. 2008, in Handbook of Star Forming Regions, Vol. I, ed. B. Reipurth, 693
Graciá-Carpio, J., García-Burillo, S., Planesas, P., Fuente, A., & Usero, A. 2008, A&A, 479, 703
Grasdalen, G. L., Strom, K. M., & Strom, S. E. 1973, ApJ, 184, L53
Greene, T. P., Wilking, B. A., Andre, P., Young, E. T., & Lada, C. J. 1994, ApJ, 434, 614
Habing, H. J. 1968, Bull. Astron. Inst. Netherlands, 19, 421
Hatchell, J., & Fuller, G. A. 2008, A&A, 482, 855
Heiderman, A., Evans, II, N. J., Allen, L. E., et al. 2010, ApJ, 723, 1019
Heyer, M., Krawczyk, C., Duval, J., & Jackson, J. M. 2009, ApJ, 699, 1092
Hill, T., Motte, F., Didelon, P., et al. 2011, A&A, 533, A94
Hollenbach, D. J., Takahashi, T., & Tielens, A. G. G. M. 1991, ApJ, 377, 192
Ikeda, N., Sunada, K., & Kitamura, Y. 2007, ApJ, 665, 1194
Inutsuka, S.-I., & Miyama, S. M. 1997, ApJ, 480, 681
Jessop, N. E., & Ward-Thompson, D. 2000, MNRAS, 311, 63
Kennicutt, Jr., R. C. 1989, ApJ, 344, 685
Könyves, V., André, P., Men'shchikov, A., et al. 2015, A&A, 584, A91
Kramer, C., Cubick, M., Röllig, M., et al. 2008, A&A, 477, 547
Lada, E. A. 1992, ApJ, 393, L25
Lada, C. J., Lombardi, M., & Alves, J. F. 2010, ApJ, 724, 687
Lada, C. J., Forbrich, J., Lombardi, M., & Alves, J. F. 2012, ApJ, 745, 190
Ladd, N., Purcell, C., Wong, T., & Robertson, S. 2005, PASA, 22, 62
Langer, W. D., & Penzias, A. A. 1993, ApJ, 408, 539
Larson, R. B. 1981, MNRAS, 194, 809
Lee, C. W., & Myers, P. C. 1999, ApJS, 123, 233
Leroy, A. K., Bigiel, F., Hughes, A., et al. 2016, in From Interstellar Clouds to Star-Forming Galaxies: Universal Processes?, eds. P. Jablonka, P. André, & F. van der Tak, IAU Symp., 315, 175
Longmore, S. N., Bally, J., Testi, L., et al. 2013, MNRAS, 429, 987
Mamajek, E. E. 2008, Astron. Nachr., 329, 10
Maury, A. J., André, P., Men'shchikov, A., Könyves, V., & Bontemps, S. 2011, A&A, 535, A77
Megeath, S. T., Gutermuth, R., Muzerolle, J., et al. 2012, AJ, 144, 192
Meijerink, R., Spaans, M., & Israel, F. P. 2007, A&A, 461, 793
Molinari, S., Swinyard, B., Bally, J., et al. 2010, A&A, 518, L100
Motte, F., André, P., & Neri, R. 1998, A&A, 336, 150
Muench, A. A., Lada, C. J., Luhman, K. L., Muzerolle, J., & Young, E. 2007, AJ, 134, 411
Myers, P. C. 1983, ApJ, 270, 105
Myers, P. C. 1998, ApJ, 496, L109
Myers, P. C. 2009, ApJ, 700, 1609
Myers, P. C., Mardones, D., Tafalla, M., Williams, J. P., & Wilner, D. J. 1996, ApJ, 465, L133
Nutter, D., & Ward-Thompson, D. 2007, MNRAS, 374, 1413
Ortiz-León, G. N., Dzib, S. A., Kounkel, M. A., et al. 2017, ApJ, 834, 143
Pety, J., Guzmán, V. V., Orkisz, J. H., et al. 2017, A&A, 599, A98
Roy, A., André, P., Palmeirim, P., et al. 2014, A&A, 562, A138
Schisano, E., Rygl, K. L. J., Molinari, S., et al. 2014, ApJ, 791, 27
Schneider, S., & Elmegreen, B. G. 1979, ApJS, 41, 87
Schneider, N., Csengeri, T., Bontemps, S., et al. 2010, A&A, 520, A49
Schneider, N., André, P., Könyves, V., et al. 2013, ApJ, 766, L17
Schneider, N., Bontemps, S., Motte, F., et al. 2016, A&A, 591, A40
Shimajiri, Y., Kitamura, Y., Nakamura, F., et al. 2015a, ApJS, 217, 7
Shimajiri, Y., Sakai, T., Kitamura, Y., et al. 2015b, ApJS, 221, 31
Shirley, Y. L. 2015, PASP, 127, 299
Shuping, R. Y., Vacca, W. D., Kassis, M., & Yu, K. C. 2012, AJ, 144, 116
Tsuboi, M., Tadaki, K.-I., Miyazaki, A., & Handa, T. 2011, PASJ, 63, 763
Usero, A., Leroy, A. K., Walter, F., et al. 2015, AJ, 150, 115
Vutisalchavakul, N., Evans, II, N. J., & Heyer, M. 2016, ApJ, 831, 73
Ward-Thompson, D., Scott, P. F., Hills, R. E., & André, P. 1994, MNRAS, 268, 276
Wu, J., Evans, II, N. J., Gao, Y., et al. 2005, ApJ, 635, L173

Appendix A: Complementary figures and tables

Figures A.1–A.9 are complementary figures. The optical depths of the HCN (1–0) and HCO^+ (1–0) lines in each A_V bin are listed in Table A.1. Table A.2 summarizes the definition of each notation used in this paper.

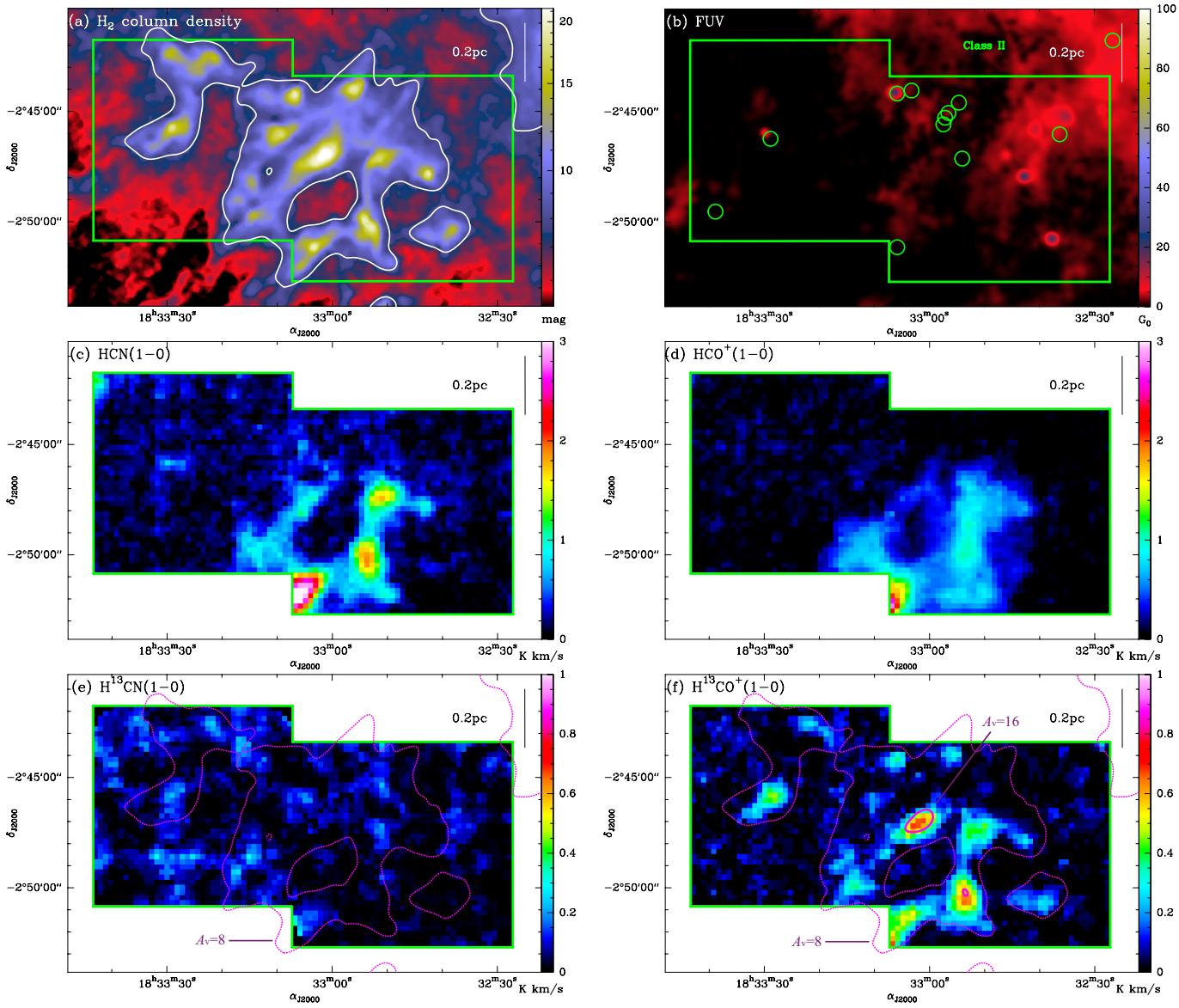

Fig. A.1. Same as Fig. 1, but for Aquila/cold. The H_2 column density map of the Aquila region is from *Herschel* Gould Belt Survey (HGBS) data (André et al. 2010; Könyves et al. 2015). The white contour in *panel a* and magenta dotted contours in *panels e* and *f* indicate the $A_V = 8$ level derived from the *Herschel* column density map smoothed to 40″ resolution. In *panel f*, the magenta solid contour indicates the rough A_V column density level above which significant $H^{13}CO^+$ (1–0) emission is detected, i.e., $A_V = 16$.

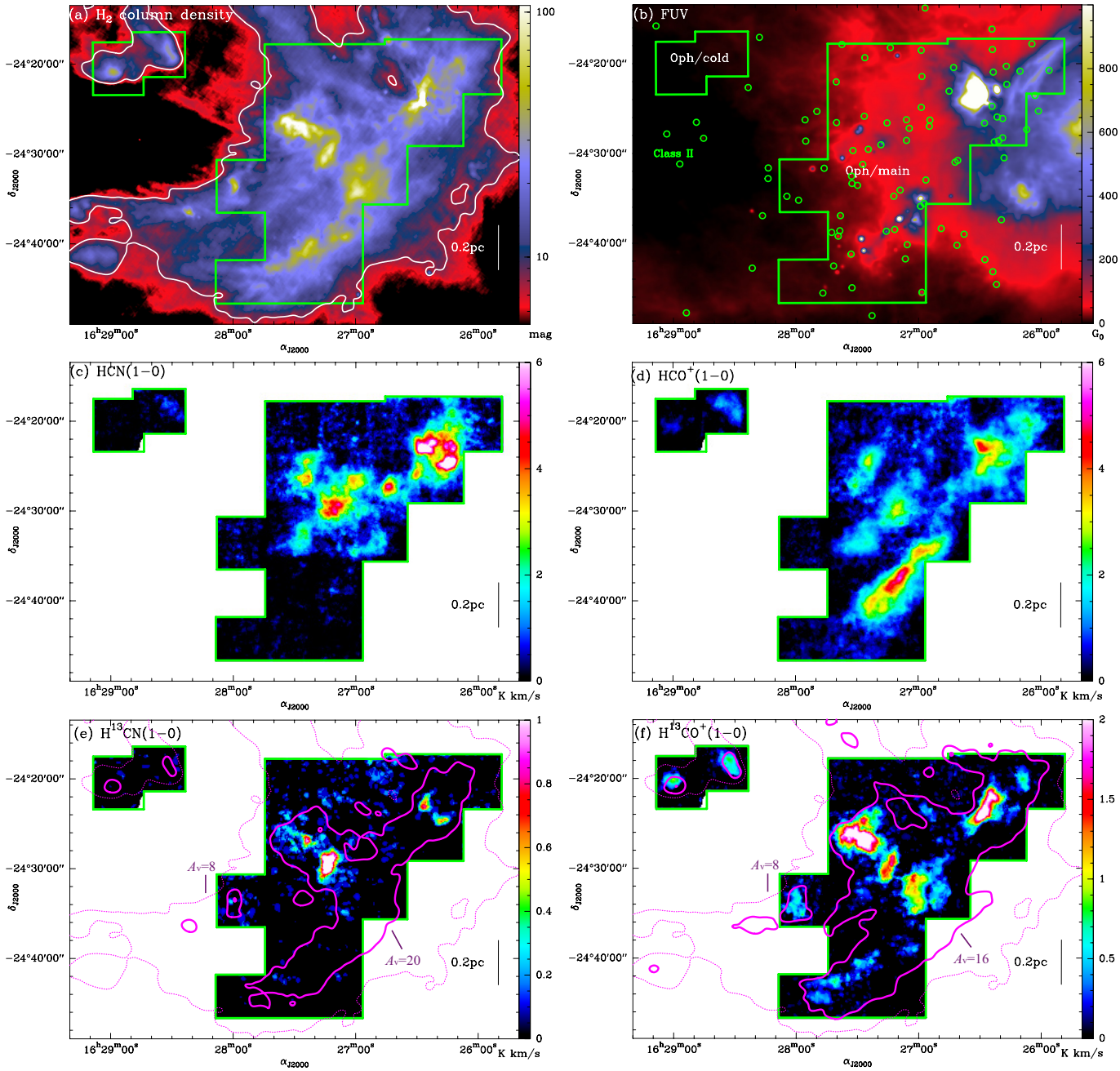

Fig. A.2. Same as Fig. 1, but for Ophiuchus. The H_2 column density map of the Ophiuchus region is from HGBS data (Ladjelate et al., in prep.). The angular resolutions of HCN, HCO^+, and $H^{13}CO^+$, and $H^{13}CN$ maps are 50″, 50″, 50″, and 60″. The white contour in *panel a* and magenta dotted contours in *panels e* and *f* indicate the $A_V = 8$ level derived from the *Herschel* column density map smoothed to 50″ resolution. In *panels e* and *f*, the magenta solid contour indicates the rough A_V column density level above which significant line emission is detected, i.e., $A_V = 20$ for $H^{13}CN$ (1–0) and $A_V = 16$ for $H^{13}CO^+$ (1–0).

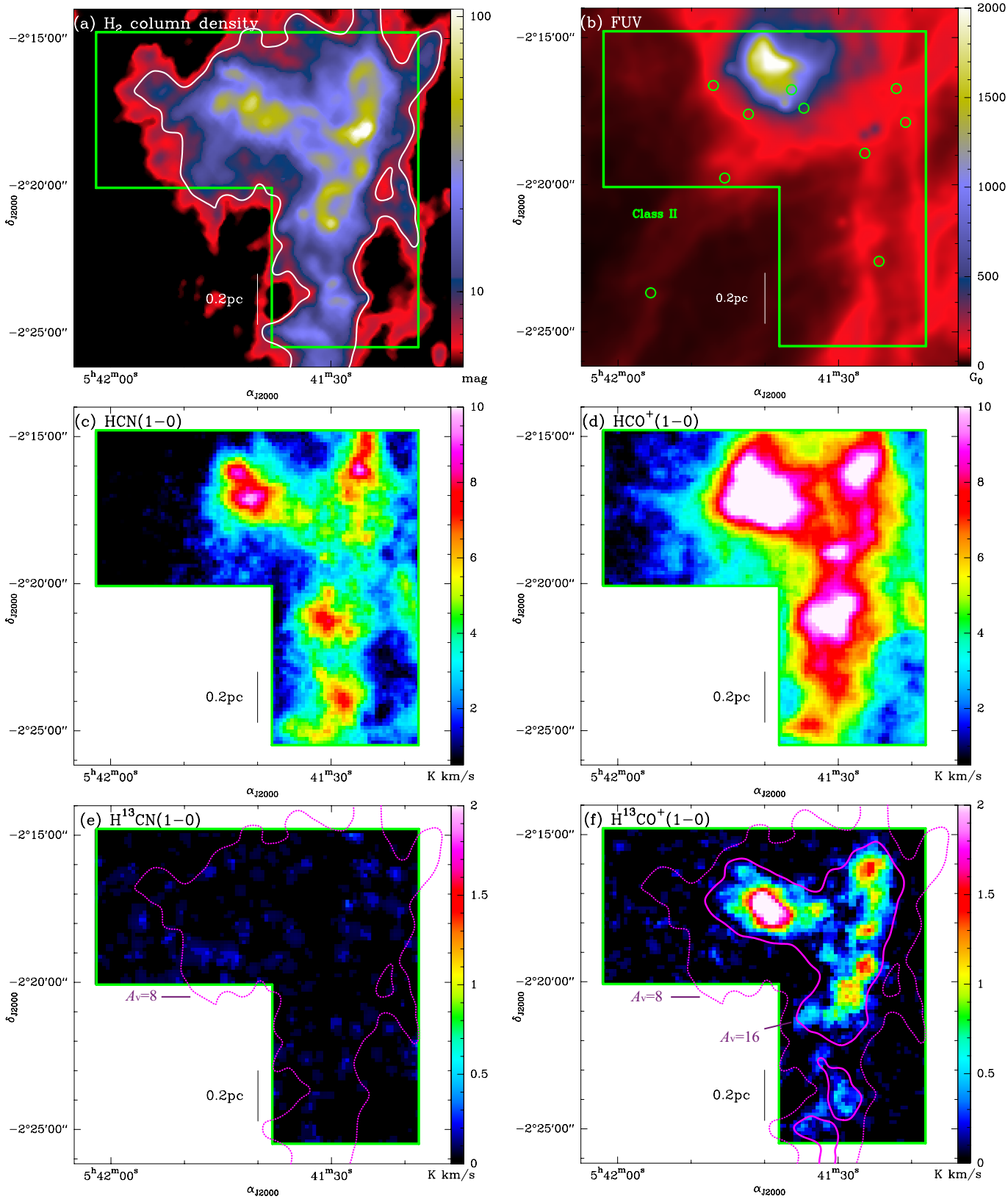

Fig. A.3. Same as Fig. 1, but for NGC 2023 in Orion B. The H_2 column density map of the Orion B region is from HGBS data (Könyves et al., in prep.; see also Schneider et al. 2013). The angular resolutions of HCN, HCO^+, and $H^{13}CO^+$, and $H^{13}CN$ maps are 30″, 30″, 30″, and 40″. The white contour in *panel a* and magenta dotted contours in *panels e* and *f* indicate the $A_V = 8$ level derived from the *Herschel* column density map smoothed to 30″ resolution. In *panel f*, the magenta solid contour indicates the rough A_V column density level above which significant $H^{13}CO^+$ (1–0) emission is detected, i.e., $A_V = 16$.

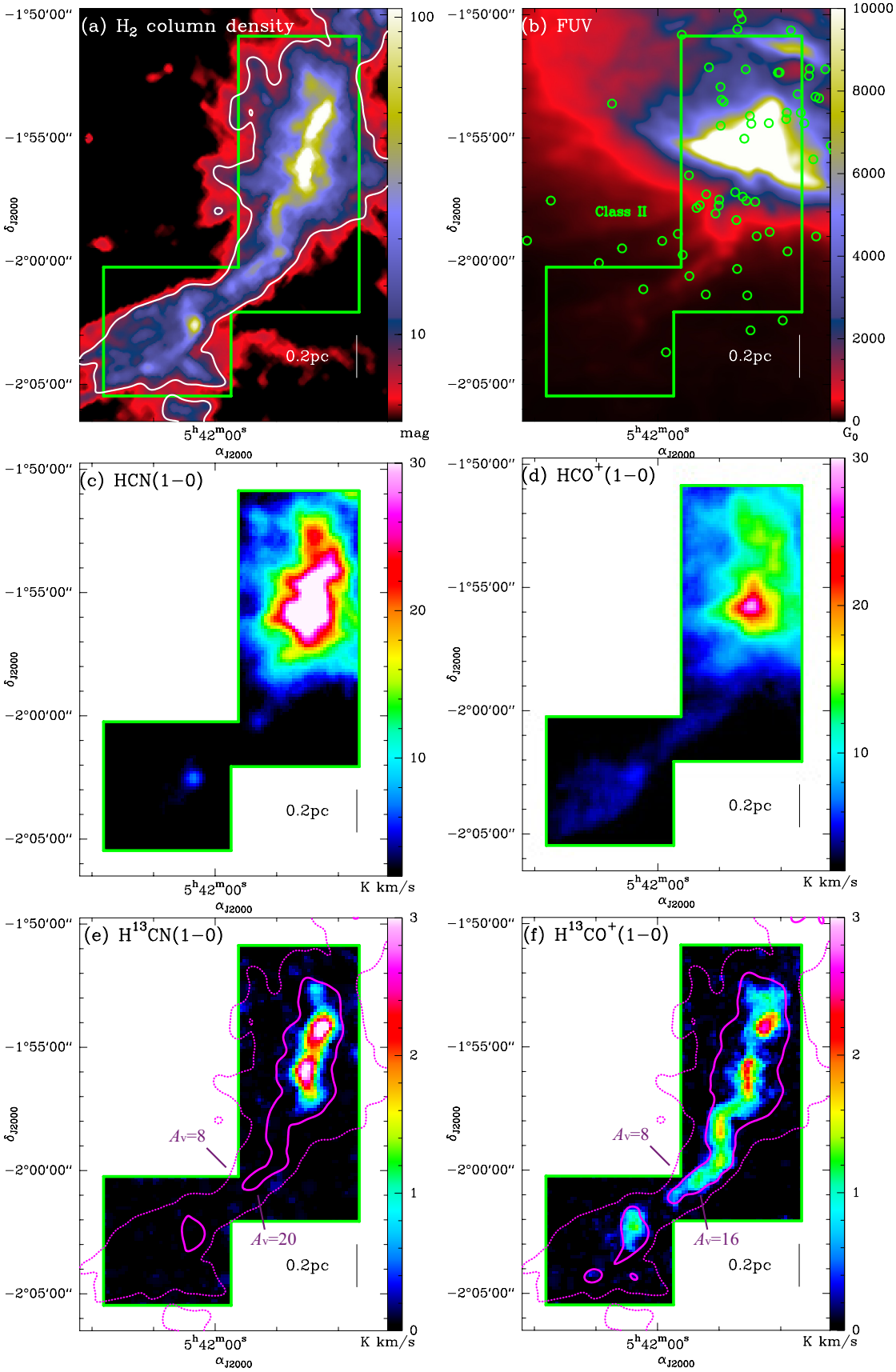

Fig. A.4. Same as Fig. 1, but for NGC 2024 in Orion B. The H_2 column density map of the Orion B region is from HGBS data (Könyves et al., in prep.; see also Schneider et al. 2013). The angular resolutions of HCN, HCO^+, and $H^{13}CO^+$, and $H^{13}CN$ maps are 30″, 30″, 30″, and 40″. The white contour in *panel a* and magenta dashed contours in *panels e* and *f* indicate the $A_V = 8$ level derived from the *Herschel* column density map smoothed to 30″ resolution. In *panels e* and *f*, the magenta solid contour indicates the rough A_V column density level above which significant line emission is detected, i.e., $A_V = 20$ for $H^{13}CN$ (1–0) and $A_V = 16$ for $H^{13}CO^+$ (1–0).

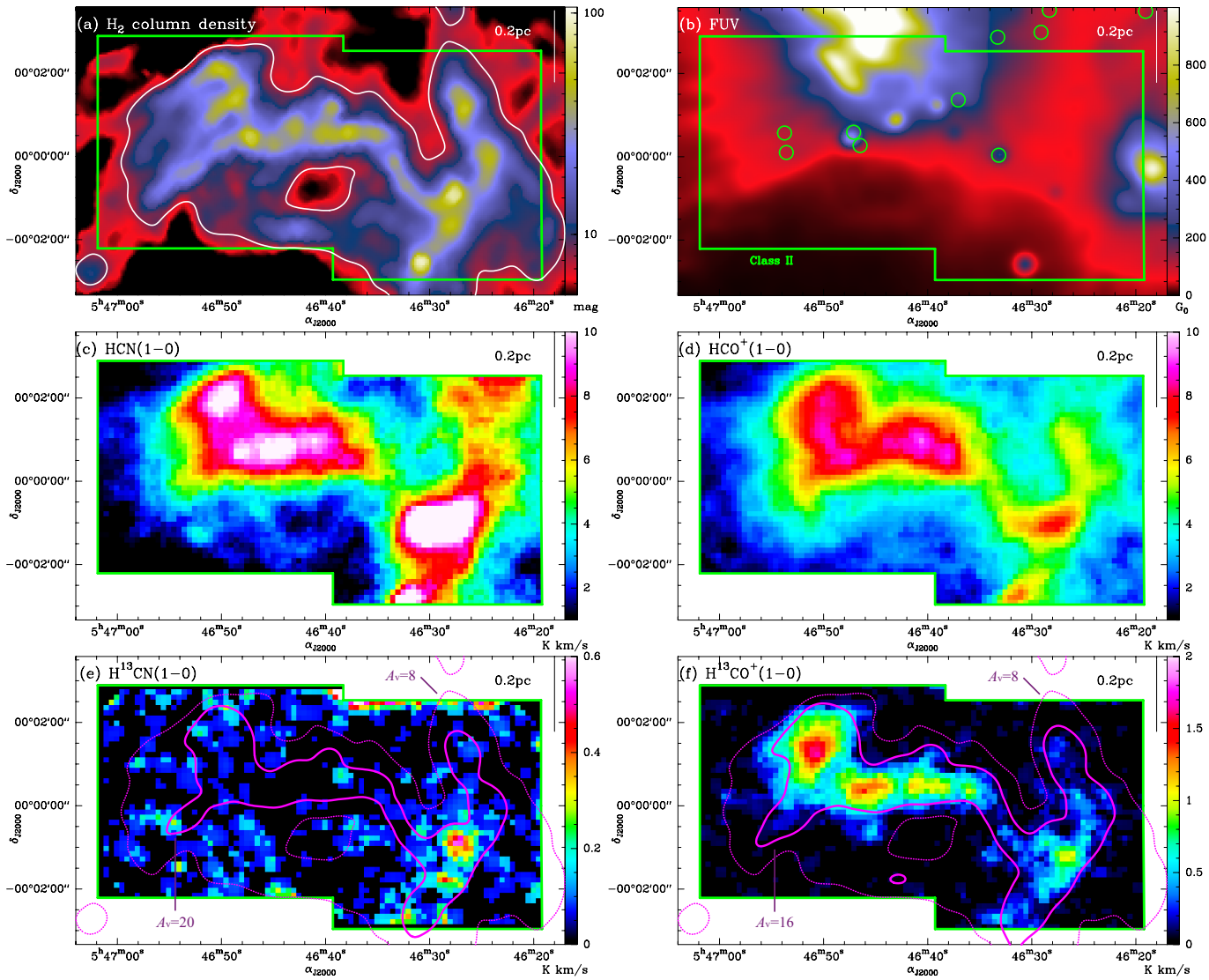

Fig. A.5. Same as Fig. 1, but for NGC 2068 in Orion B. The H_2 column density map of the Orion B region is from HGBS data (Könyves et al., in prep.; see also Schneider et al. 2013). The angular resolutions of HCN, HCO^+, and $H^{13}CO^+$, and $H^{13}CN$ maps are 30″, 30″, 30″, and 40″. The white contour in *panel a* and magenta dashed contours in *panels e* and *f* indicate the $A_V = 8$ level derived from the *Herschel* column density map smoothed to 30″ resolution. In *panels e* and *f*, the magenta solid contour indicates the rough A_V column density level above which significant line emission is detected, i.e., $A_V = 20$ for $H^{13}CN$ (1–0) and $A_V = 16$ for $H^{13}CO^+$ (1–0).

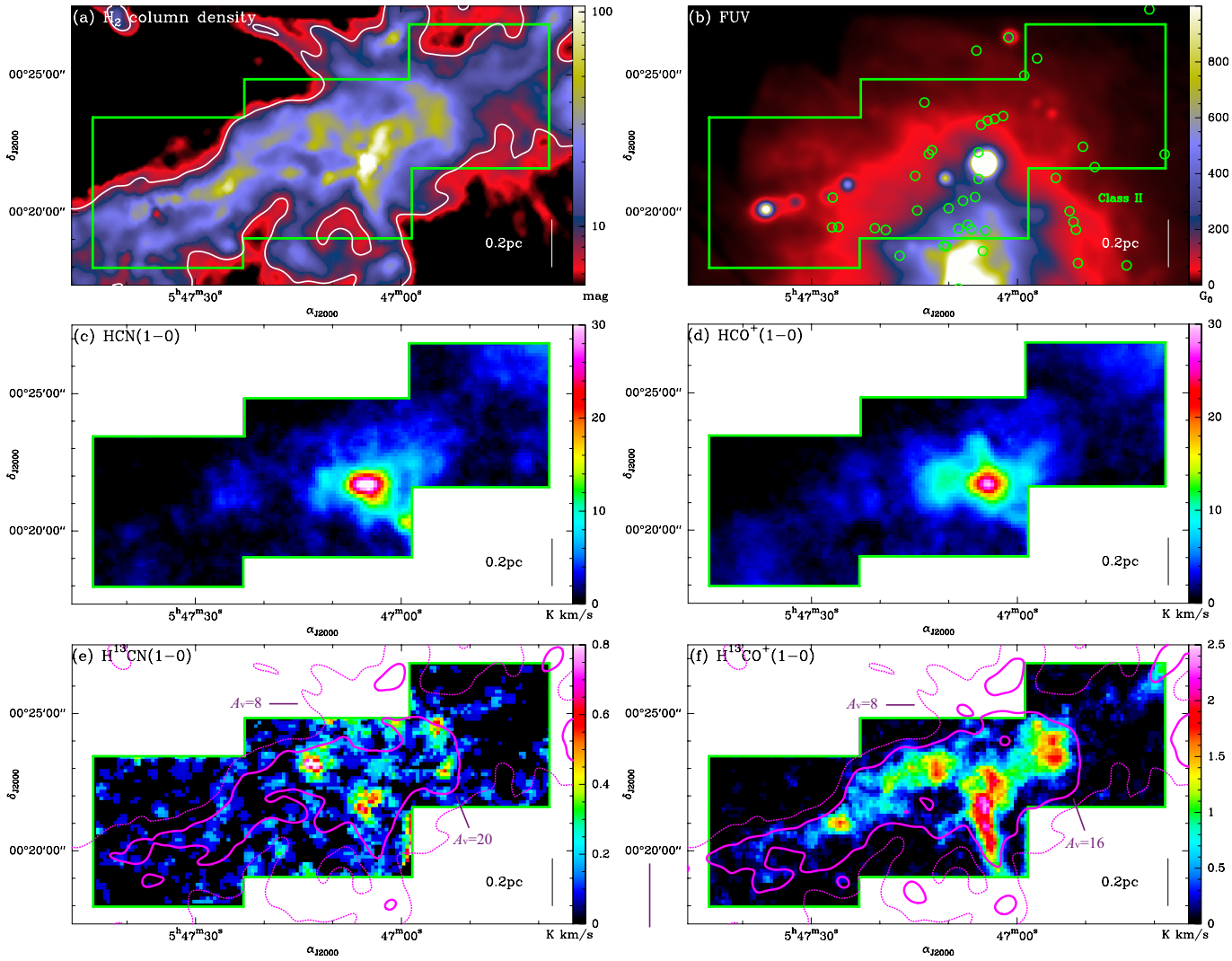

Fig. A.6. Same as Fig. 1, but for NGC 2071 in Orion B. The H_2 column density map of the Orion B region is from HGBS data (Könyves et al., in prep.; see also Schneider et al. 2013). The angular resolutions of HCN, HCO^+, and $H^{13}CO^+$, and $H^{13}CN$ maps are 30″, 30″, 30″, and 40″. The white contour in *panel a* and magenta dashed contours in *panels e* and *f* indicate the $A_V = 8$ level derived from the *Herschel* column density map smoothed to 30″ resolution. In *panels e* and *f*, the magenta solid contour indicates the rough A_V column density level above which significant line emission is detected, i.e., $A_V = 20$ for $H^{13}CN$ (1–0) and $A_V = 16$ for $H^{13}CO^+$ (1–0).

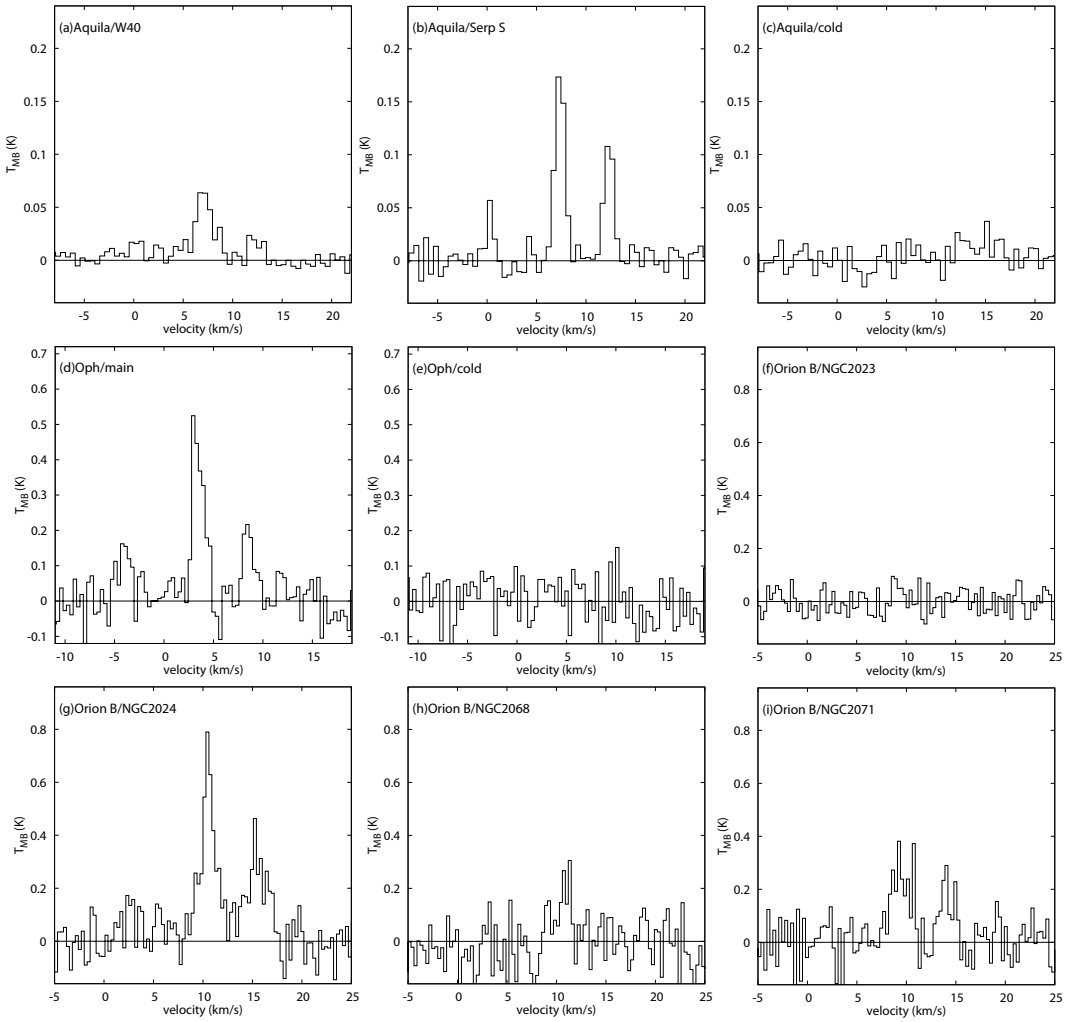

Fig. A.7. Comparison of $H^{13}CN$ spectra averaged over pixels where has $\geq 5\sigma$ emission at *a)* Oph/main; *b)* Oph/cold; *c)* Aquila/W40; *d)* Aquila/Serp. South; *e)* Aquila/cold; *f)* NGC 2023; *g)* NGC 2024; *h)* NGC 2068; and *i)* NGC 2071. For Oph/cold, Aquila/cold, and NGC 2023, the $H^{13}CN$ emission is not detected. Thus, we show the spectra averaged over observing area.

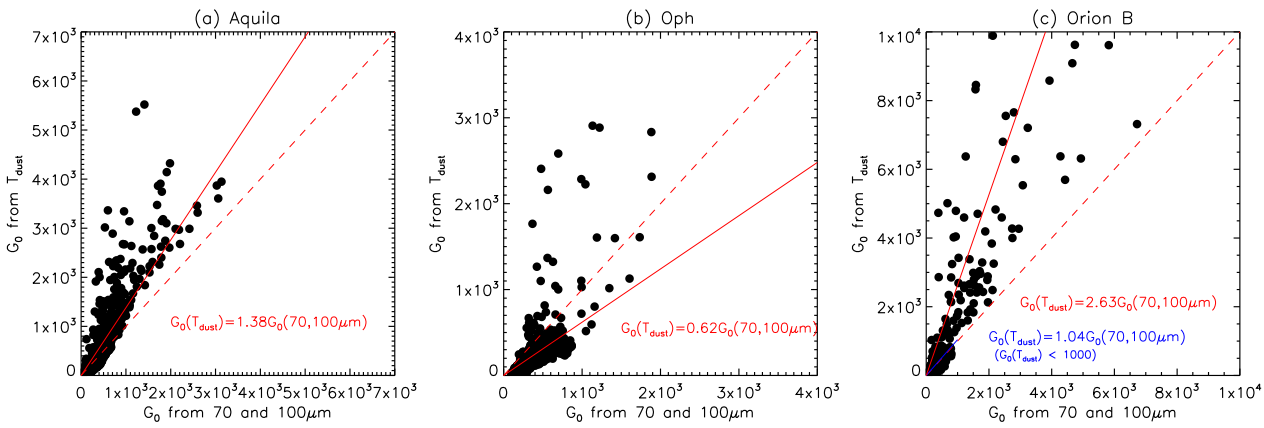

Fig. A.8. Pixel to pixel correlation between the G_0 value estimated from $T_{\rm dust}$, $G_0(T_{\rm dust})$, using Eqs. ((11)–(13)) map and G_0 values estimated from *Herschel* 70 and 100 μm data, $G_0(70, 100\ \mu{\rm m})$, using Eqs. ((9), (10)) toward *a)* Aquila; *b)* Ophiuchus; *c)* Orion B. The dashed red lines indicate $G_0(T_{\rm dust}) = G_0(70, 100\ \mu{\rm m})$. The solid red lines indicate the best-fit results: $G_0(T_{\rm dust}) = (1.38 \pm 0.01) \times G_0(70, 100\ \mu{\rm m})$ for Aquila, $G_0(T_{\rm dust}) = (0.62 \pm 0.01) \times G_0(70, 100\ \mu{\rm m})$ for Ophiuchus, and $G_0(T_{\rm dust}) = (2.63 \pm 0.09) \times G_0(70, 100\ \mu{\rm m})$ for Orion B. The blue lines in *panel c* indicate the best-fit result for pixels with $G_0(T_{\rm dust}) < 1000$: $G_0(T_{\rm dust}) = (1.04 \pm 0.02) \times G_0(70, 100\ \mu{\rm m})$.

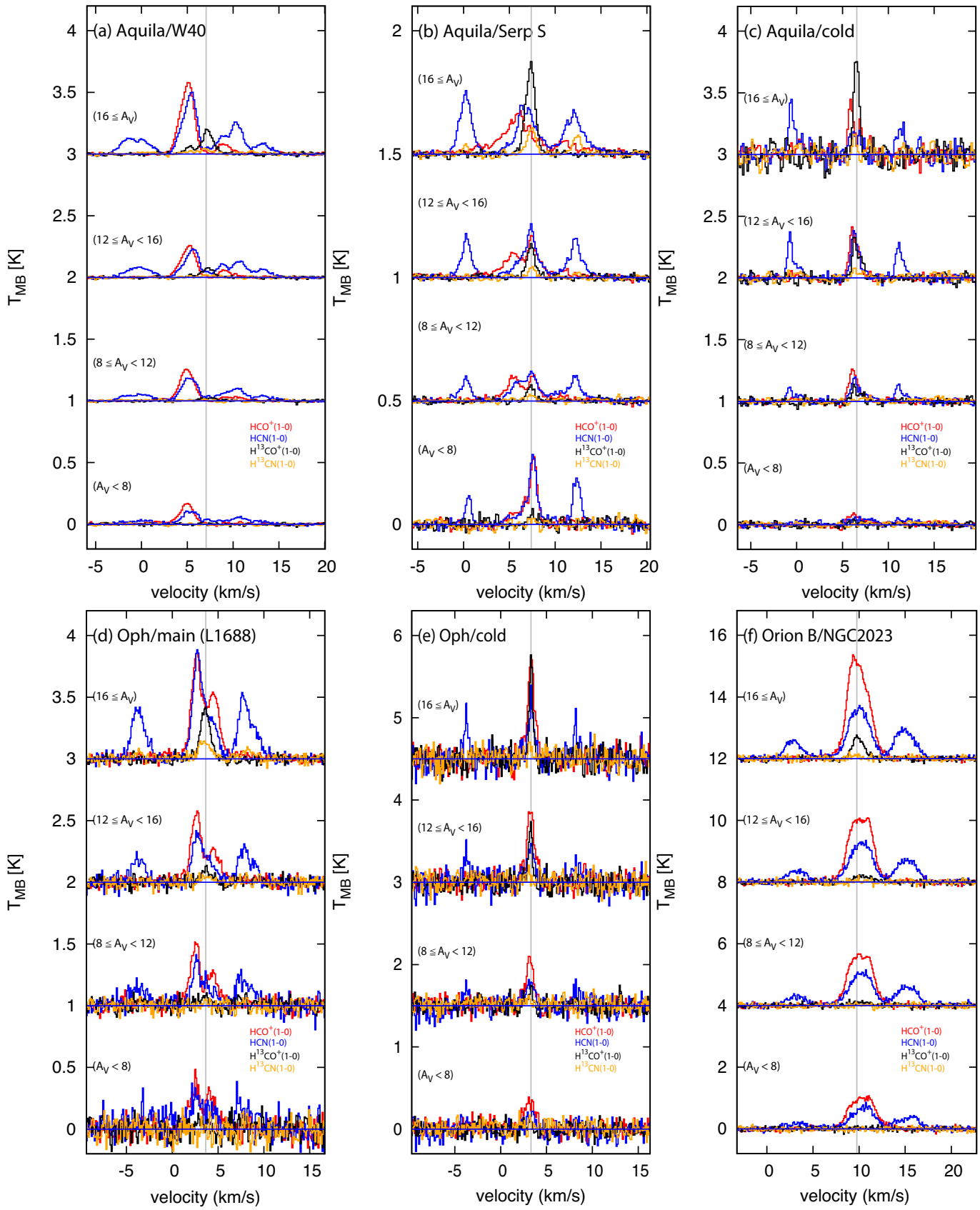

Fig. A.9. Comparison of the HCO^+ (1–0, red), HCN (1–0, blue), $H^{13}CO^+$ (1–0, black), and $H^{13}CN$ (1–0, orange) spectra averaged over the observed area in each A_V range for *a)* Aquila/W40; *b)* Aquila/Serp-South; *c)* Aquila/cold; *d)* Oph/main; *e)* Oph/cold; *f)* Orion B/NGC 2023; *g)* Orion B/NGC 2024; *h)* Orion B/NGC 2068; and *i)* Orion B/NGC 2071. In each panel, the vertical grey line marks the peak velocity of the $H^{13}CO^+$ line toward the $16 \leq A_V$ area, and the spectra shown *from top to bottom* correspond to the $16 \leq A_V$, $12 \leq A_V < 16$, $8 \leq A_V < 12$, and $A_V < 8$ areas, respectively.

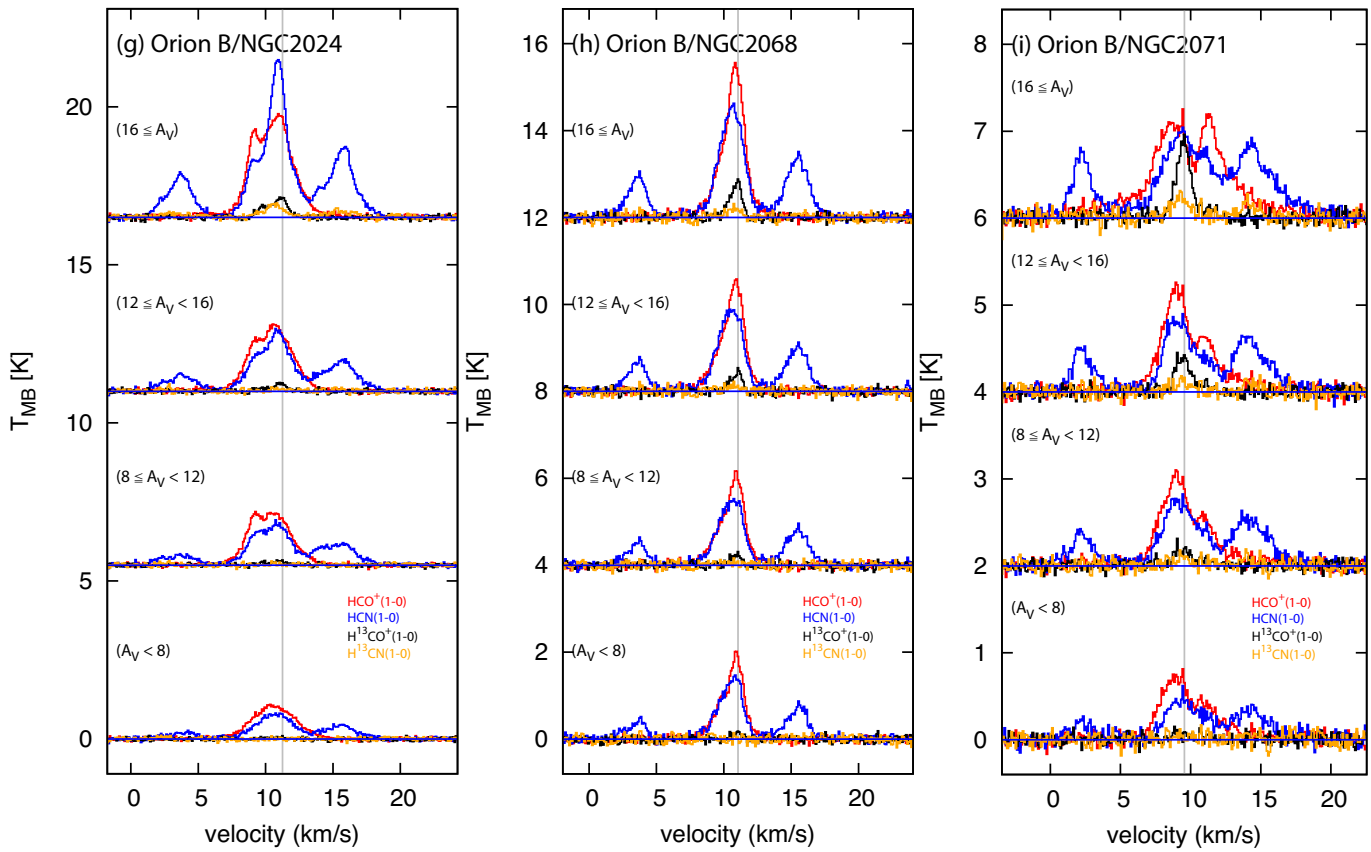

Fig. A.9. continued.

Table A.1. Optical depths of the HCN (1–0) and HCO^+ (1–0) lines[†] .

Region	Molecule	$A_V < 8$	$8 \leq A_V < 12$	$12 \leq A_V < 16$	$16 \leq A_V$
Aquial/W40	HCN(1–0)	–[‡]	–[‡]	35	»1[SA]
	HCO^+(1–0)	–[‡]	159	»1[SA]	»1[SA]
Aquila/Serp S	HCN(1–0)	–[‡]	–[‡]	17	103
	HCO^+(1–0)	17	67	102	»1[SA]
Aquila/cold	HCN(1–0)	–[‡]	–[‡]	16	135
	HCO^+(1–0)	–[‡]	51	124	»1[SA]
Oph/main (L1688)	HCN(1–0)	–[‡]	–[‡]	–[‡]	14
	HCO^+(1–0)	–[‡]	–[‡]	80	»1[SA]
Oph/cold	HCN(1–0)	–[‡]	–[‡]	‡ ‡	–[‡]
	HCO^+(1–0)	–[‡]	–[‡]	128	»1[SA]
Orion B/NGC2023	HCN(1–0)	–[‡]	–[‡]	112	12
	HCO^+(1–0)	–[‡]	10	8	18
Orion B/NGC2024	HCN(1–0)	–[‡]	–[‡]	–[‡]	6
	HCO^+(1–0)	–[‡]	7	10	14
Orion B/NGC2068	HCN(1–0)	–[‡]	–[‡]	–[‡]	8
	HCO^+(1–0)	–[‡]	11	16	20
Orion B/NGC2071	HCN(1–0)	–[‡]	–[‡]	–[‡]	24
	HCO^+(1–0)	–[‡]	21	29	»1[SA]

Notes. [(†)] The spectra in Fig. A.9 are used to derive the intensities. [(‡)] The emission of the rare species is not detected. [(SA)] The intensity of the normal species is weaker than that of the rare species due to the self-absorption effect.

Table A.2. Definition of each notation used in the paper.

Quantity	Notation	Meaning
Surface area	$A_{\rm mol}^{\rm detect}$	Area where the $H^{13}CO^+$ or $H^{13}CN$ emission has been detected.
	$A_{Herschel}^{A_V>8}$	Area above $A_V = 8$ according to the *Herschel* column density map in each observed cloud
Cloud radius	$R_{\rm mol}^{\rm detect}$	Equivalent radius of the area where $H^{13}CO^+$ or $H^{13}CN$ emission has been detected in each cloud.
	$R_{Herschel}^{A_V>8}$	Equivalent radius of the area above $A_V = 8$ in each observed cloud (according to the *Herschel* column density map).
Velocity width	$dV_{\rm FWHM}$	FWHM velocity width at each pixel
	$dV_{\rm mol}^{\rm detect}$	FWHM velocity width estimated from the spectrum averaged over the area where $H^{13}CO^+$ or $H^{13}CN$ emission has been detected.
	$dV_{\rm mol}^{A_V>8}$	Scaled FWHM velocity width using $dV_{\rm mol}^{A_V>8} = dV_{\rm mol}^{\rm detect}\left(\frac{R_{Herschel}^{A_V>8}}{R_{\rm mol}^{\rm detect}}\right)^{0.5}$
Mass	$M_{\rm VIR,mol}^{\rm detect}$	Virial mass of the portion of each cloud where $H^{13}CO^+$ or $H^{13}CN$ emission has been detected.
	$M_{\rm VIR,mol}^{A_V>8}$	Virial mass of the region above $A_V = 8$ in each observed cloud.
	$M_{Herschel}^{\rm mol-detect}$	Dense gas mass estimated from the *Herschel* column density map of the area where $H^{13}CO^+$ or $H^{13}CN$ emission has been detected.
	$M_{Herschel}^{A_V>8}$	Dense gas mass estimated from the *Herschel* column density map for the area above $A_V = 8$ in each observed cloud.
	$M_{\rm dense,mol}$	Dense gas mass estimated from molecular luminosity conversion factor ($M_{\rm dense,mol} = \alpha_{Herschel-{\rm mol}}^{\rm fit} L_{\rm mol}$).
Virial ratio	$\mathcal{R}_{\rm VIR,mol}^{\rm detect,}$	Virial mass ratio of the portion of the cloud where the $H^{13}CO^+$ or $H^{13}CN$ emission has been detected ($\mathcal{R}_{\rm VIR,mol}^{\rm detect} = M_{\rm VIR,mol}^{\rm detect}/M_{Herschel}^{\rm mol-detect}$).
	$\mathcal{R}_{\rm VIR,mol}^{A_V>8}$	Virial mass ratio of the region above $A_V = 8$ in each observed cloud ($\mathcal{R}_{\rm VIR,mol}^{A_V>8} = M_{\rm VIR,mol}^{A_V>8}/M_{Herschel}^{A_V>8}$).
Star-formation rate	$SFR_{\rm YSO}$	Star formation rate estimated from the number count of YSOs.
	$SFR_{\rm prestellar}$	Star formation rate estimated from the number count of prestellar cores.
HCN conversion factor	$\alpha_{\rm HCN}$	Conversion factor from HCN(1–0) luminosity to dense gas mass.
	$\alpha_{Herschel-{\rm HCN}}$	Empirical $\alpha_{\rm HCN}$ factor derived for the target nearby clouds using *Herschel* mass estimates as references ($\alpha_{Herschel-{\rm HCN}} = M_{Herschel}^{A_V>8}/L_{\rm HCN}$).
	$\alpha_{Herschel-{\rm HCN}}^{\rm fit}$	$\alpha_{\rm HCN}$ conversion factor obtained from the relation $\alpha_{Herschel-{\rm HCN}}^{\rm fit} = 496 \times G_0^{-0.24}$.
	$\alpha_{Herschel-{\rm HCN}}^{\rm fit'}$	$\alpha_{\rm HCN}$ conversion factor obtained from the relation $\alpha_{Herschel-{\rm HCN}}^{\rm fit'} = 0.13 \times G_0^{-0.095} \times \alpha_{Herschel-{\rm HCN}}^{\rm fit}$.
	$\alpha_{\rm GS04-HCN}$	$\alpha_{\rm HCN}$ conversion factor assumed in Gao & Solomon (2004a).
	$\alpha_{\rm Wu05-HCN}$	$\alpha_{\rm HCN}$ conversion factor obtained in Wu et al. (2005).
	$\alpha_{\rm GB12-HCN}$	$\alpha_{\rm HCN}$ conversion factor obtained in García-Burillo et al. (2012).
	$\alpha_{\rm Usero-HCN}$	$\alpha_{\rm HCN}$ conversion factor obtained in Usero et al. (2015).
HCO^+ conversion factor	$\alpha_{Herschel-{\rm HCO^+}}$	$\alpha_{\rm HCO^+}$ conversion factor obtained toward each observed sub region in the present study ($\alpha_{Herschel-{\rm HCO^+}} = M_{Herschel}^{A_V>8}/L_{\rm HCO^+}$).
	$\alpha_{Herschel-{\rm HCO^+}}^{\rm fit}$	$\alpha_{\rm HCO^+}$ conversion factor obtained by the relation $\alpha_{Herschel-{\rm HCO^+}}^{\rm fit} = 689 \times G_0^{-0.24}$.